

ABSTRACT

RATZLAFF, CHELSEA ROBYN. Detector Response Function for a Germanium Strip Type Detector/Imager. (Under the direction of John Mattingly).

Coded aperture imagers using high purity germanium (HPGe) dual sided strip detectors are a technology that has become increasingly popular in the past ten years. Pioneers in this field include Klaus Ziock et al. who developed the initial design of this type of detector and Fenimore and Cannon in the field of coded aperture imaging. Ethan Hull of the company PHDS is responsible for the detector design found in this project. These technologies combine superior spectral resolution with position resolution to produce spectroscopic images of unknown radiation sources. This has potential impacts in many fields from homeland security to medical imaging. This research expands on an interpolation method by M. Guttormsen et al. to create a detector response function. The response function is pre-calculated using Monte Carlo transport, and uses MATLAB and Python scripts that pull from a log of gamma ray interactions generated with MCNPX-PoliMi for individual source energies and radial distances. MCNPX-PoliMi, a Monte Carlo transport code, was used to create a model of the dual sided, electrode strip, cylindrical HPGe detector located at Oak Ridge National Laboratory and created by the company PHDS. The detector was shown to be radially symmetric, therefore cutting down on computational time by replacing the two dimensional (x,y) pixel coordinates with a single radial position on the detector. The response function interpolation was validated by comparing the MCNPX-PoliMi direct calculations with the interpolated detector response function for a single source energy. In addition, a direct calculation of the Ba-133 gamma spectrum was also compared to the pre-calculated interpolated detector response function. The interpolated spectrum maintained the general features of the spectrum but did exhibit some error compared to the direct calculation. The error appears in the re-binning of the interpolated spectrum and could be addressed by using finer energy bins for the response function.

© Copyright 2014 by Chelsea Ratzlaff

All Rights Reserved

Detector Response Function for a Germanium Strip Type Detector/Imager

by
Chelsea Robyn Ratzlaff

A thesis submitted to the Graduate Faculty of
North Carolina State University
in partial fulfillment of the
requirements for the degree of
Master of Science

Nuclear Engineering

Raleigh, North Carolina

2014

APPROVED BY:

Robin Gardner

David Lalush

John Mattingly (Committee Chair)

DEDICATION

To Lille Mu, who sat and watched me write the entire thesis.

BIOGRAPHY

Chelsea Robyn Ratzlaff was born in Tulsa, Oklahoma on April 29, 1989. She grew up in Asheville, NC and received her B.S. in Nuclear Engineering in May, 2012 from North Carolina State University.

ACKNOWLEDGMENTS

Most importantly, I would like to thank the NCSU Nuclear Engineering Department and specifically Dr. John Mattingly for giving me this great opportunity. Special thanks to Oak Ridge National Laboratory (ORNL) for supporting me during this research and especially Matthew Blackston at ORNL. In addition, I would like to thank Dr. Tony Nettleton for his continued support, Casper Holmgren for his programming insight, and Wesley Holmes for his help and moral support. And, of course, I would like to say thanks to my friends and family for putting up with me during my long hours of stress and coursework. Especially Lille Mu, who was with me through it all.

TABLE OF CONTENTS

LIST OF TABLES	v
LIST OF FIGURES	vi
Chapter 1: Introduction	1
1.1 Background and Motivation	1
1.2 Scope of Thesis	2
Chapter 2: Germanium Detectors and Response Functions	6
2.1 Germanium Detector Fundamentals	6
2.2 Gamma Spectroscopy	10
2.2.1 Spectral Features	10
2.2.2 Energy Resolution	16
2.3 Coded Aperture Imaging with HPGe Strip Detector	19
2.4 Detector Dimensions and Setup	24
2.5 Detector Response Functions	26
Chapter 3: Procedures for Calculating the Detector Response Function	29
3.1 MCNPX-PoliMi Simulations	29
3.2 Creating Detector Image	32
3.3 Determining Source Beam Radius	34
3.4 Determining Energies to Run	39
3.5 Creating Input Files and Running Script on 32 CPUs	40
3.6 Proving Radial Symmetry of the Detector	42
3.7 Interpolating Separate Features of the Spectrum	48
3.8 Re-binning Interpolated Energy Bins to MCNP Energy Bins	56
Chapter 4: Results	57
4.1 Calculated Response Function	57
4.2 Single Energy and Radial Position Interpolated Response Function	62
4.3 Ba-133 Decay Spectrum Using Interpolation Method	66
Chapter 5: Conclusions	78
References	81

LIST OF TABLES

Table 2.1: Properties of Germanium as a Semiconductor	8
Table 3.1: Important Detector Dimensions in MCNPX-PoliMi	29
Table 3.2: Count Error for Comparing X and Y Directions	44
Table 4.1: Gamma Ray Energies and Intensities for ¹³³Ba	67

LIST OF FIGURES

Figure 2.1: Semi-Conductor Detector Mechanics	7
Figure 2.2: Gamma-Ray Spectrum Features	11
Figure 2.3: Klein-Nishina Kernel	13
Figure 2.4: Compton Continuum Shape	14
Figure 2.5: Energy Resolution	16
Figure 2.6: Pinhole Camera Diagram	19
Figure 2.7: A Uniformly Redundant Array Coded Aperture	20
Figure 2.8: Steps Involved in Coded Aperture Imaging	21
Figure 2.9: Side Measurement of HPGe Strip Detector	22
Figure 2.10: Front View Measurements of Detector	23
Figure 2.11: Detector Setup	24
Figure 2.12: Detector Setup Cont'd.	25
Figure 2.13: Germanium Detector Response Function Example	28
Figure 3.1: Front (a) and Back (b) Detector Views	30
Figure 3.2: Front (a) and Back (b) Tilted Detector Views	30
Figure 3.3: Detector/Source Setup.....	31
Figure 3.4: MCNPX PoliMi Log File Coordinates & Energy Deposited	33
Figure 3.5: HPGe Strip Detector Image Running 10^9 Particles	34
Figure 3.6: Setup for Determining Beam Width	35
Figure 3.7: Detector Face Beam Width Visualization	36
Figure 3.8: Center Pixel Counts vs. Source Beam Width	37
Figure 3.9: Far Left Pixel Subset Counts vs. Source Beam Width	37
Figure 3.10: Top Pixel Subset Counts vs. Source Beam Width	38
Figure 3.11: Energy vs FWHM for HPGe Detector	40
Figure 3.12: Input Card Generating Algorithm	41
Figure 3.13: Algorithm of MCNPX-PoliMi across N CPUs	42
Figure 3.14: Distribution of Pixel Counts in the Y Direction	43
Figure 3.15: Distribution of Pixel Counts in X Direction	43
Figure 3.16: Spectral Changes with X-Position	45
Figure 3.17: Spectral Changes with Y-Position	46
Figure 3.18: Comparing SLERP Method & MCNPX-PoliMi Calculation	47
Figure 3.19: Linear Scale w/ SLERP Method & MCNPX-PoliMi Calculation ..	48
Figure 3.20: Detector Response Function Data Building Algorithm	50
Figure 3.21: MCNPX-PoliMi Output File Log	51
Figure 3.22: Algorithm for Determining Feature from Particle History	52
Figure 3.23: Interpolation Counts from Lower and Upper Spectra	54

Figure 3.24: Sweep-Style Re-binning Algorithm	57
Figure 4.1: Response Function for the HPGe detector at 0.25 cm Radius	58
Figure 4.2: Response Function for the HPGe detector at 0.25 cm Radius, Log ..	59
Figure 4.3: Response Function for the HPGe detector at 4.25 cm Radius	60
Figure 4.4: Response Function for the HPGe detector at 4.25 cm Radius, Log ..	61
Figure 4.5: Photon Effects at Different Energy and in Different Material	62
Figure 4.6: Spectrum vs Interpolated w/o Re-binning, Linear	63
Figure 4.7: Spectrum vs Interpolated Spectrum w/o Re-binning, Log	64
Figure 4.8: Spectrum vs Interpolated Spectrum w/ Re-binning, Linear	65
Figure 4.9: Spectrum vs. Interpolated Spectrum w/ Re-binning, Log	66
Figure 4.10: Decay Scheme for ^{133}Ba to ^{133}Cs	67
Figure 4.11: ^{133}Ba Decay Spectrum Using MCNPX-PoliMi	68
Figure 4.12: ^{133}Ba Decay Spectrum Using MCNPX-PoliMi (Log Scale)	68
Figure 4.13: Germanium Spectrum of ^{133}Ba	69
Figure 4.14: ^{133}Ba Spectrum Rebinned, Radius=0.25cm, Linear	70
Figure 4.15: ^{133}Ba Spectrum Rebinned, Radius=0.25cm, Log	71
Figure 4.16: ^{133}Ba Spectrum Rebinned, Radius=2.25 cm, Linear	72
Figure 4.17: ^{133}Ba Spectrum Rebinned, Radius=2.25 cm, Log	73
Figure 4.18: ^{133}Ba Spectrum Rebinned, Radius=2 cm, Linear	74
Figure 4.19: ^{133}Ba Spectrum Rebinned, Radius=2 cm, Log	75
Figure 4.20: ^{133}Ba Spectrum Rebinned, Radius=2 cm, Linear	76
Figure 4.21: ^{133}Ba Spectrum Rebinned, Radius=2 cm, Log	77

Chapter 1: Introduction

1.1 Background and Motivation

Coded aperture imaging with germanium strip detectors is a new technique that has been developed in the past ten years. These types of detectors can pinpoint the location of the radiation by using directional information, in addition to having better energy resolution than earlier designs based on inorganic scintillators [34]. However, several drawbacks have impeded the acceptance of these imagers into practice. Portability, cost, and time to create high quality images have kept this technology out of regular field use in portal monitoring [2]. Adding an aperture in the form of a uniformly redundant array is a direct way to create even higher quality images [2].

Radiation portal monitoring (RPM) has become an important aspect of nuclear security and safeguards worldwide. RPM provides a passive means to detect potentially dangerous nuclear materials in cargo by using radiation detectors that carriers slowly pass by, one at a time [1]. The data from the detectors, which essentially is a time sensitive profile of the carriers, either triggers an alarm or is collected, stored, and analyzed [2]. Currently, to detect gamma rays and neutrons from potentially harmful nuclear material in these portals, polyvinyl-toluene (PVT) based plastic scintillation gamma ray and ^3He detectors are used, respectively [2]. The combined number of false alarms for all US ports of entry is around 200,000 annually [7]. False alarms can be caused by certain materials like granite which naturally contain radioactivity and household products such as cat litter and some ceramics, among other common products [2]. Alarmingly, the U.S. Government Accountability Office (GAO) tested the current portal monitoring system and was able to smuggle two dirty bombs

worth of nuclear material across the ports [10]. It is clear that the technology in radiation portal monitoring systems needs to be improved. Better detection of weak sources in the background, locating the source position, and identifying its constituents can aid in decreasing false alarms- all things that the detector in this project is able to do.

Increased spatial resolution with coded apertures has been used with organic scintillators [37]. The goal of this research was to ultimately use this increase in spatial resolution in a Compton imager. Coded apertures are limited by the position resolution of the detector it uses, and this use of the Compton imager can overcome this problem [37]. These inorganic scintillator detectors have better energy resolution than traditional alkali-halide scintillators and can be built at a much cheaper price than germanium detectors [37]. However, though these detectors have high spatial resolution, capable of 1.0 mm voxels, their energy resolution is significantly worse than that of HPGe detectors.

Furthermore, the work on detector response functions using the CEARDRFs code from Gardner et al. creates accurate DRFs for scintillation detectors [20]. The gamma ray transport algorithms and benchmark experiments have helped to lay a foundation for creating detector response function methods, even in high purity germanium (HPGe) type detectors.

1.2 Scope of Thesis

This work includes computational modeling and analysis of a specific coded aperture imager that uses HPGe strip detectors. The work is broken down into three main contributions:

- Modeling the detector in MCNPX PoliMi

- Creating a detector response function
- Interpolating the response function and re-binning the results

All of these stages are done computationally using a combination of MATLAB, MCNPX PoliMi, Python, and Haskell.

HPGe based coded aperture gamma ray imagers are a new technology that can detect and identify nuclear materials with high energy and spatial resolution. Ziock et al. was the pioneer in HPGe-based coded aperture gamma ray imagers [3]. In particular, Ethan Hull et al. of PHDS created this specific detector. These imagers are capable of acquiring high resolution spectroscopic images to detect and identify nuclear materials. The drawbacks of this technology include its high cost and poor portability of HPGe detectors. Some of his research led to the creation of a highly portable system of these HPGe detectors, despite needing to be cryogenically cooled [3]. Since Germanium detectors are semi-conductors, they must be cryogenically cooled because at higher temperatures electrons have enough energy to cross the band gap into the conduction band of the germanium crystals which creates noise in the spectroscopic data [15]. In addition, even more work on these imagers has been developed by Ziock et al. where a similar cross-stripped planar germanium based detector was used to create pixel-by-pixel spectra with a fully de-convolved coded aperture [18] [34]. This means that the energy spectrum is available at each individual pixel with a high number of energy bins because of the high detector resolution- presenting a large computational task. Instead of creating a pre-calculated detector response function that can be interpolated, as in this project, images in Ziock's work were built one at a time using pre-

imaged arrays of the response with the coded aperture intact [3]. Similarly, this project used pre-generated spectra but only for the strip detector itself, not including the coded aperture.

Much of the work done on coded aperture imaging with uniformly redundant arrays was originally created by Fenimore and Cannon [4]. Their work created the autocorrelation functions and de-convolution methods that have the advantageous properties of image reconstruction. This includes high angular resolution but still a relatively high efficiency of gamma rays coming through to be detected [4]. In their work, multiple holes arranged in a uniformly redundant array form many overlapping images of the same object that can be decoded and reconstructed yielding a very high quality image. In addition, their works have shown that the anti-mask pattern of the uniformly redundant array negates background radiation when this data is overlaid on top of one another [4].

Detector Response Functions (DRF) act as a library of different spectra with different source energies and positions. In other words, by pre-calculating the response function, a synthetic spectrum for identification is rapidly generated. By implementing an interpolation method of the response function, computational time is greatly reduced compared to Monte Carlo calculation of a specific source energy and position. One way to unfold gamma ray continuum spectra was developed by Guttormsen et al. [33]. This method interpolates different features of gamma ray spectra such as the Compton scattering parts, full energy peaks, and backscatter peaks, etc.- all identifiable by set equations. In this specific case, an unfolding method estimating the shape of the Compton continuum, single and double escape peaks, and pair-production annihilation peaks were not considered. This project uses aspects of the interpolation method but is not concerned with pair production

effects such as escape peaks and annihilation peaks. These effects are hard to track and are not present in MCNPX PoliMi. The method described in this work focuses on the full energy peak, backscatter peak, and Compton edge/continuum stretching.

One of the limiting factors of this technology is the time it takes to create a high quality image. By looking at the HPGe strip detector without the aperture and creating a pre-calculated detector response function, a spectrum can be generated for an arbitrary position and energy much faster than by using a Monte Carlo simulation to determine the gamma ray spectrum of an unknown source.

The novel parts of this work contributing to HPGe coded aperture imagers include:

- Proving radial symmetry of the detector to decrease computational time to characterize the entire detector
- Implementing a linear interpolation method of individual features of the gamma ray spectra detector response function
- Decreasing computational time by using this interpolation method to characterize unknown radiation sources

These new contributions for the field of HPGe strip detector coded aperture imaging and decrease in computational time can have effects in a broad range of fields from homeland security to the development of new medical imaging devices.

Chapter 2: Germanium Detectors and Response Functions

2.1 Germanium Detector Fundamentals

For semiconductor detectors, germanium and silicon are the best detector mediums. HPGe is germanium that has undergone reduction of impurities by zone refining and then slowly grown into crystals from the melted feedstock to be used as detector material [15]. This type of detector is called a semi-conductor and uses electron-hole pairs as charge carriers made by the interacting gamma rays in the detector medium. Gamma rays can excite electrons into the conduction band from the deeper valence bands in the detector medium. This can sometimes cause secondary ionization, increasing the number of electron hole pairs. This raises an electron to the conduction band which leaves behind a “hole” in the valence band [15]. The conductivity in the detector depends on the band gap, or the difference in energy between the valence band and the conduction band. In an electrically neutral semiconductor detector, these holes in the valence band equal the electrons in the conduction band. When a current is applied across the detector, these electron-hole pairs drift in opposite directions towards the electrical contacts because electrons are negatively charged and the holes act in response as a positive charge resulting in a count in the detector (Figure 2.1) [16].

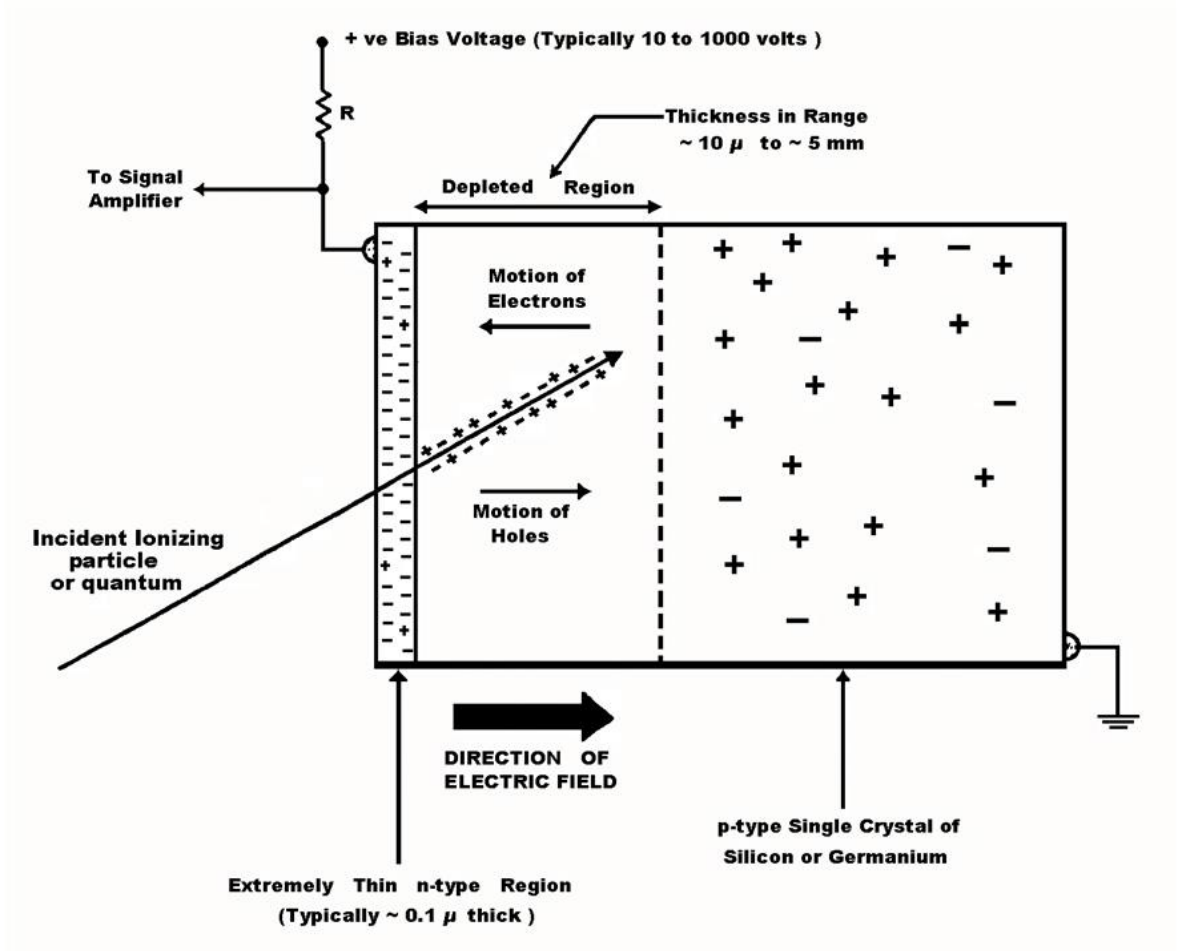


Figure 2.1: Semi-Conductor Detector Mechanics [32]

Sometimes, the band gap is so large between the valence and conduction bands that at normal temperatures, electrons are not able to reach the conduction band. This is called an insulator (band gap is greater than 10 eV). Conversely, if the band gap is nonexistent and the conduction and valence band overlap, this is called a conductor. As mentioned before, in a semiconductor detector, the band gap is small enough (about 1 eV) that thermal energy can initiate the electrons to reach the conduction band [15]. Because electrons can move through

the band gap with only thermal energy, there will always be electron hole pairs in the detector medium. However, because thermal energy is present, there will always be a thermal leakage current. As the temperature increases, the electron/hole concentration increases and the band gap also decreases. This is the reason germanium type detectors have to be cryogenically cooled, thus getting rid of the leakage current (noise) at regular temperatures [15]. Important semiconductor properties are shown in Table 2.1.

Table 2.1 Properties of Germanium as a Semiconductor [15]

<u>Property</u>	<u>Germanium</u>
Atomic Number	32
Atomic Weight	72.6
Density	5330 kg/m ³
Energy Gap @ (300 K)	0.67 eV
Energy Gap @ (0 K)	0.75 eV
Average Energy per electron-hole pair (77 K)	2.96 eV

There are two types of semiconductor detectors, intrinsic and extrinsic. Intrinsic germanium semiconductors have atoms that share 4 covalent bonds with nearby atoms and the electrons equal the number of holes. However, germanium detectors are typically doped with an impurity that has 5 or 3 covalent bonds so the electron hole pairs will not be the same, called an extrinsic type semiconductor [15]. Therefore, one of the bonds in the impurity with the 5 covalent bonds will not be part of a chemical bond and is weakly bound,

allowing it to move easily into the conduction band without leaving behind an electron hole [15]. This is a donor impurity, called an n-type (negative) extrinsic semiconductor (germanium, for instance). Conversely, if the impurity has 3 covalent bonds, one of the electrons is not bonded and the host can covalently bond at this site, subsequently creating a hole. This is an acceptor impurity, called a p-type (positive) extrinsic semiconductor detector. A p-n junction is created when a p-type and an n-type semiconductor are put together [15]. Since the n-type has extra electrons and the p-type has extra holes, the electrons and holes will diffuse into each other from high to low concentrations making a p-n junction that has a small electrical potential difference [15]. An applied electric field will collect these electron hole pairs. When a positive voltage is applied to the n-type electrode and a negative voltage to the p-type electrode, this “reverse bias” slows down the electron/hole diffusion and a depletion region is formed at this junction where electron/hole pairs are scarce [15]. Most of these pairs will be at the donor and acceptor sites creating an electrical potential difference that is affected by the voltage of this bias. If radiation enters the depletion region, new electron/hole pairs will be created and are pulled to the electrodes with the reverse bias voltage electric field. The hole mobility of semiconductor detectors is close to the electron mobility so charge collection only takes a short amount of time, creating a faster time response than other detectors [15]. HPGe detectors are doped with both n and p-type impurities at the cathode and anode and have large depletion regions (10mm-100mm) [15].

Though semiconductor detectors operate similarly to gas filled detectors, there are some important differences. Because semiconductor detectors are made out of solid media, they intrinsically have a higher atomic number, which, for gamma detection, has a higher

photoelectric to Compton ratio and much higher intrinsic efficiency due to its greater density. Additionally, compared to gas filled detectors, they can operate in a vacuum, are insensitive to magnetic fields, and have faster pulse rise times [15]. Semiconductors also have faster pulse rise times than scintillator detectors. Furthermore, compared to scintillator detectors, semiconductor detectors have greater energy resolution and have a linear response with energy over a much greater range [15].

However, there are a few disadvantages of using a semiconductor detector. Semiconductors use crystals which are hard to manufacture causing them to be much more expensive, especially for larger detectors that have greater efficiency. Germanium and silicon detectors must also be cryogenically cooled to reduce thermal leakage noise.

2.2.1 Spectral Features

Because gamma-rays have no charge, they create a direct excitation of the material and therefore rely on secondary reactions in the detecting material [15]. Gamma rays can interact with material in few different ways including photoelectric absorption (photopeak), Compton scattering, and pair production [29]. An example of these features is given below (Figure 2.2).

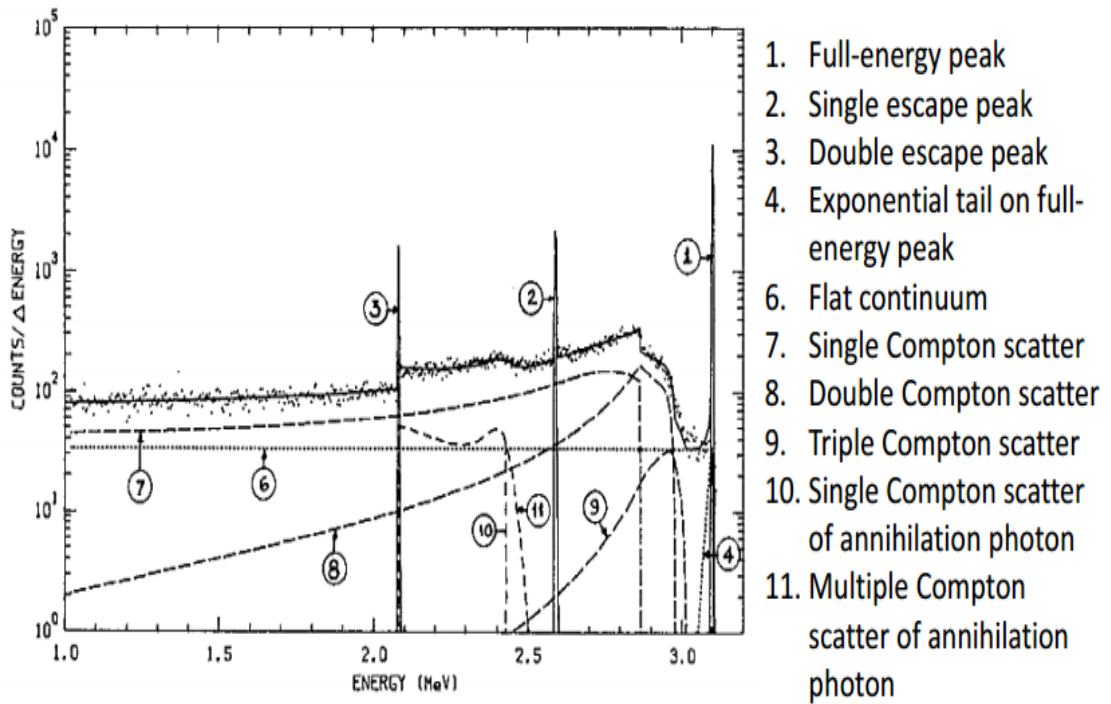


Figure 2.2: Gamma-Ray Spectrum Features [41]

Photoelectric absorption happens when a gamma ray is completely consumed by an orbital electron causing that electron to leave its orbit. As a result, an x-ray is produced from this energy when a higher energy electron falls back into this vacancy [29]. The x-ray gets absorbed unless the detector is very small.

$$T_e = E_\gamma - B \tag{1}$$

The energy of this electron is given in Equation 1 where B is the binding energy of the electron and E_γ is the energy of the incoming gamma ray. The binding energy is usually absorbed in the detector when the resulting x-ray or Auger electron is captured [15].

Compton scattering happens when a gamma ray hits an electron orbiting an atom, depositing some of its energy into the electron and then continuing on a different trajectory than before [29]. The energy is given by Equation 2. When Compton scattering occurs, the energy can range from zero to a maximum found using the electron energy and angle relationship of Compton scattering (Equation 2) where theta is 180 degrees [29].

$$E'_\gamma = \frac{E_\gamma}{1 + \frac{E_\gamma}{m_e c^2} (1 - \cos \theta)} \quad (2)$$

$$T_{e^-} = E_\gamma - E'_\gamma \quad (3)$$

E_γ is the gamma ray energy, E'_γ is the scattered gamma ray energy, m_e is the rest mass of an electron, and T_{e^-} is the kinetic energy of the electron.

The Compton continuum is caused by the partial deposition of energy in the detector from a gamma ray. The shape is based on the differential cross section of gamma rays that are Compton scattered, shown in the Klein-Nishina distribution (Figure 2.3) where larger gamma ray energies are more likely to scatter in the forward direction than those of a lower energy.

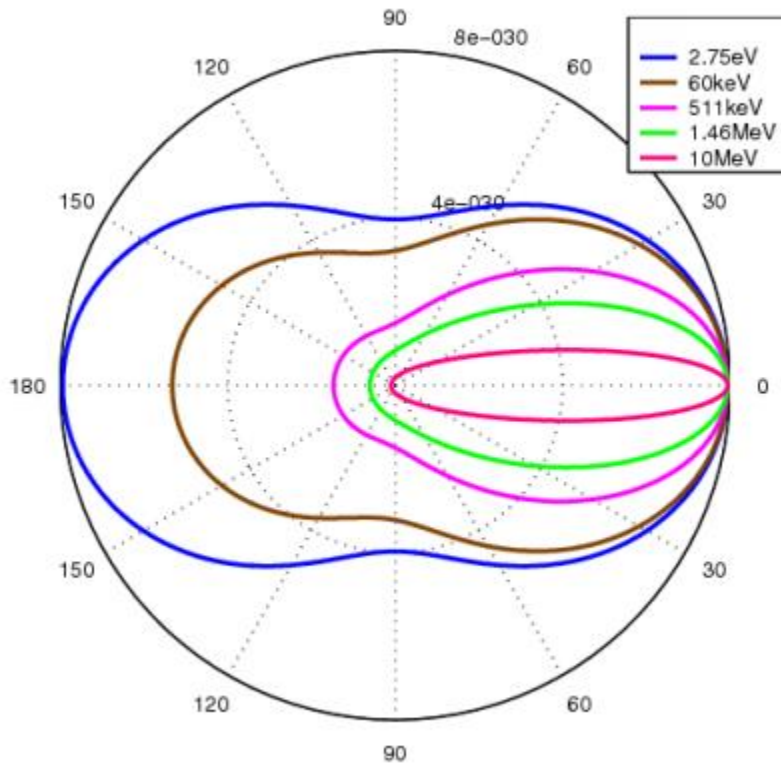


Figure 2.3: Klein-Nishina Kernel [15]

This distribution causes changes in the Compton continuum shape as shown below (Figure 2.4). As the atomic number value is increased in a detector medium, the scattering probability increases shifting the continuum upwards.

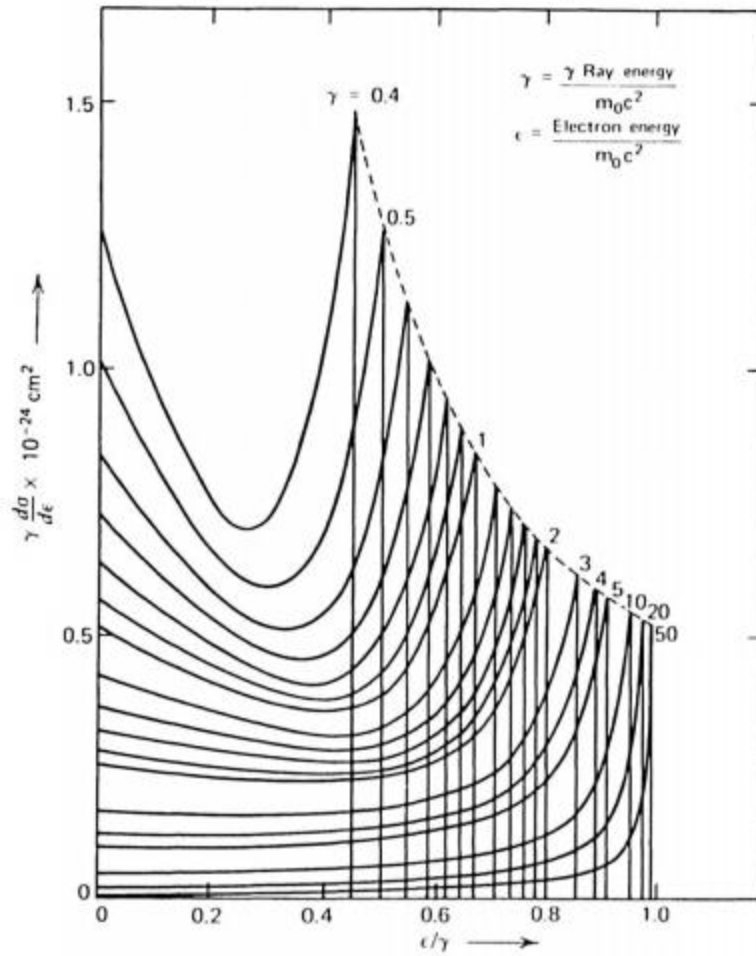


Figure 2.4: Compton Continuum Shape [15]

The energy of the Compton edge or where the maximum electron energy is located ($\theta = 180^\circ$), can be found using Equation 4 and 5.

$$E'_{\gamma\min} = \frac{E_\gamma}{1 + \frac{2E_\gamma}{m_e c^2}} \quad (4)$$

$$T_{e^-, \max} = E_\gamma - E'_{\gamma, \min} \quad (5)$$

E_γ is the gamma ray energy, m_e is the rest mass of an electron, $T_{e^-, \max}$ is the Compton edge and E'_γ is the scattered photon.

Another way that gamma rays can interact with material is through pair production. Under the influence of the nuclear Coulomb field, a gamma ray splits into an electron and a positron. This only happens with gamma rays of an energy 1.022 MeV or higher, because this is the energy of the combined rest mass of these electron/positron pair. Escape peaks occur when one or both of the annihilation photons escape the detector [15].

The backscatter peak in gamma ray spectroscopy happens when a photon has a Compton scatter in a material other than the detector first and then is absorbed in the detection medium [15]. The equation for the backscatter peak is similar to the scattered photon equation (Equation 2) but instead theta is typically close to pi, yielding Equation 6.

$$E'_\gamma = \frac{E_\gamma}{1 + \frac{2E_\gamma}{m_e c^2}} \quad (6)$$

E_γ is the gamma ray energy, m_e is the rest mass of an electron, and E'_γ is the scattered photon.

2.2.2 Energy Resolution

The measurement of resolution is usually described using Full Width Half Max (FWHM), or the width of the spectrum at half its maximum height. If this value is divided by the centroid of the peak, it should give the resolution of the peak (Equation 70 [1]). This is seen in Figure 2.5.

$$R = \frac{\Gamma}{H_0} \quad (7)$$

Γ is the FWHM and H_0 is the centroid of the peak.

The standard deviation (σ) for the resolution is shown in Equation 8.

$$\Gamma = 2\sqrt{2\ln 2} \cdot \sigma \approx 2.35\sigma \quad (8)$$

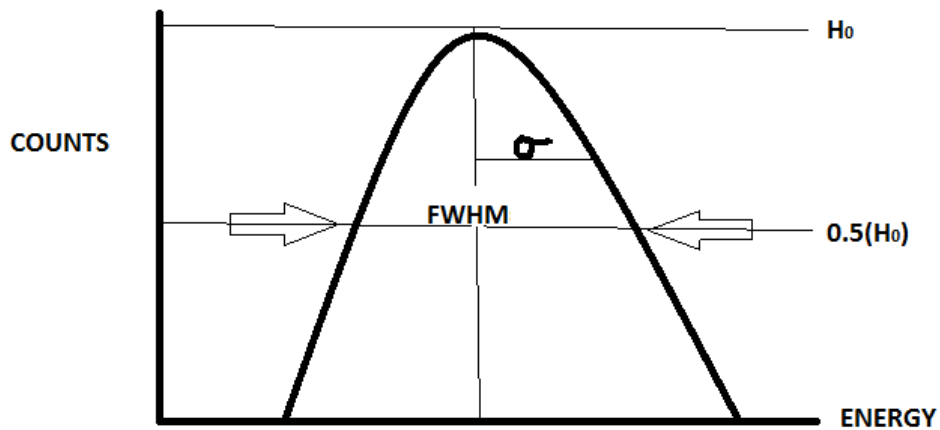


Figure 2.5: Energy Resolution

The number of information carriers, N , has variation equal to the square root of N (Equation 9) [1].

$$\sigma = \sqrt{N} \quad (9)$$

Because the resolution is affected by this variation and assuming all photons interact completely, the larger number of information carriers (N) yields better resolution. When observing resolution versus energy, the peaks tend to widen as pulse height increases but the resolution narrows. This is shown in Equation 10 and 11 [15].

$$\begin{aligned} H_0 &\propto N \\ \Gamma &= 2.35\sqrt{N} \propto \sqrt{H_0} \\ \therefore \frac{\Gamma}{H_0} &\propto \frac{1}{\sqrt{H_0}} \end{aligned} \quad (10)$$

Thus, in the statistical limit, resolution is proportional to one over the square root of the centroid energy [15].

$$\Gamma \propto \sqrt{H_0} \quad (11)$$

Energy resolution reflects the precision of the energy measurement [1]. The energy resolution is affected by three factors. The first is statistical noise from the random variation of electron/hole pairs that are produced in the detector medium (Γ_s). This is calculated using Equation 12.

$$\Gamma_s^2 = (2.35)^2 EwF \quad (12)$$

W is the amount of energy needed to make an electron hole pair, $2.35\sqrt{E}$ is the standard deviation of the random variation of charge carriers, and F is the Fano factor. The Fano factor accounts for the fact that the energy loss is not completely statistical. The Fano factor for HPGe is around 0.1 and would be 0 for no variation in the charge carriers and would be 1 for a Poisson distribution in charge carriers [15].

A ballistic deficit is another factor that decreases efficiency, and is due to incomplete charge collection (Γ_B). There is also random variation in the electronics of the system causing changes in the pulse height (Γ_E). The total of the factors affecting the resolution (Γ^2) of the system is shown in Equation 13.

$$\Gamma^2 = \Gamma_s^2 + \Gamma_B^2 + \Gamma_E^2 \quad (13)$$

In summation, germanium detectors have two main advantages, the first being that the detector medium is solid, allowing for many more collisions in less space than a gaseous detector medium. The second advantage is the increased number of charge carriers which

makes an electrical output results in the detector having much better energy resolution [15]. Germanium has a resolution that is 100 times better than most scintillators because of the greater number of charge carriers [15].

2.3 Coded Aperture Imaging with HPGe Strip Detector

Coded apertures, in their simplest form, are known as pinhole apertures [34]. Pinhole apertures provide excellent angular resolution but they do so at the cost of efficiency.

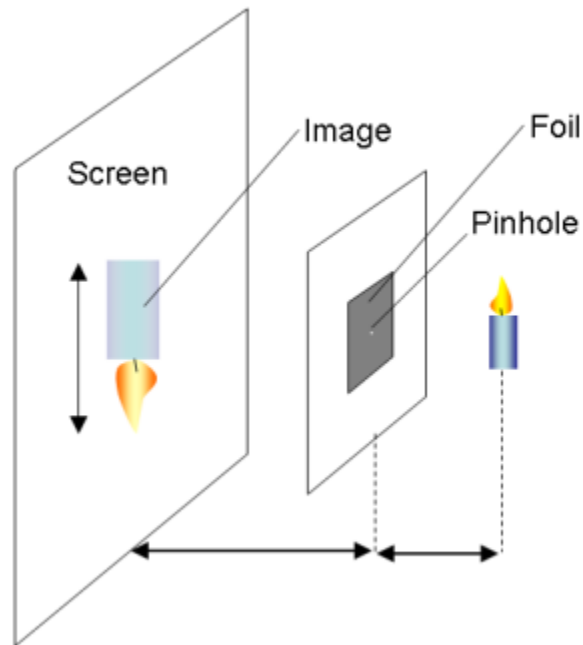


Figure 2.6: Pinhole Camera Diagram [35]

Coded apertures maintain good angular resolution but they also provide higher efficiency and a good signal-to-noise ratio (SNR) [3]. This works by scaling what the

detector sees through the aperture to the object being imaged therefore giving a particular depth of the object [3]. There is an inherent tradeoff between noise and resolution, and when a high resolution imager is used there is significant noise as a result. Reducing the size of the aperture hole increases resolution but at the same time reduces light sensitivity- adding to noise [40].

Coded apertures consist of a grid with opaque and non-opaque material for stopping gamma rays in a “mask” pattern. They can be in different arrangements, such as a semi-random uniformly redundant array. This aperture design has rotational symmetry and the anti-mask has the unique property of canceling out background radiation [3]. The uniformly redundant array in this project is shown in Figure 2.7.

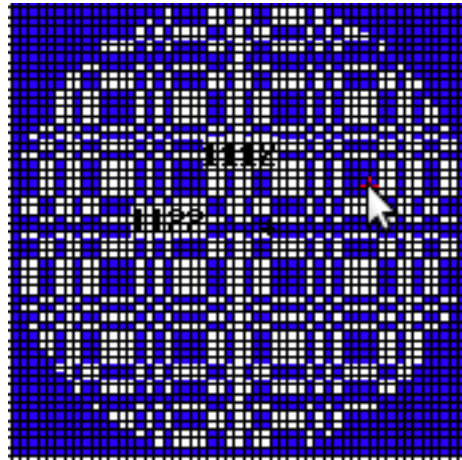


Figure 2.7: A Uniformly Redundant Array Coded Aperture [23]

The shadow created from the mask onto the detector can yield information that can be de-convolved and show the original object [18] (Figure 2.8).

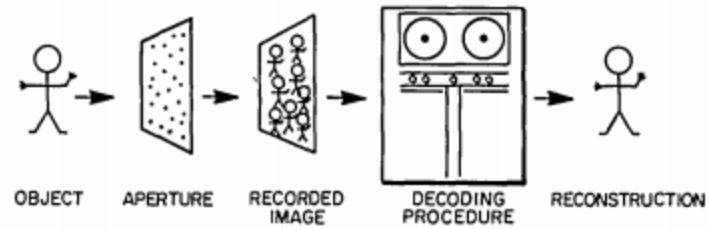


Figure 2.8: Steps Involved in Coded Aperture Imaging [4]

HPGe strip detectors have more than just superior energy resolution; they also have the ability to perform as an imager. The detector used in this project is classified as a dual sided strip detector (DSSD) because it is made up of one cylindrical piece of HPGe with electrode strips on each side. The strips are rotated 90 degrees on one side to create a grid pattern of detection area. With this design, the two dimensional position of the incident radiation interaction can be measured by coincidence. The measurements of the actual detector and strips are given in Figure 2.9 and Figure 2.10.

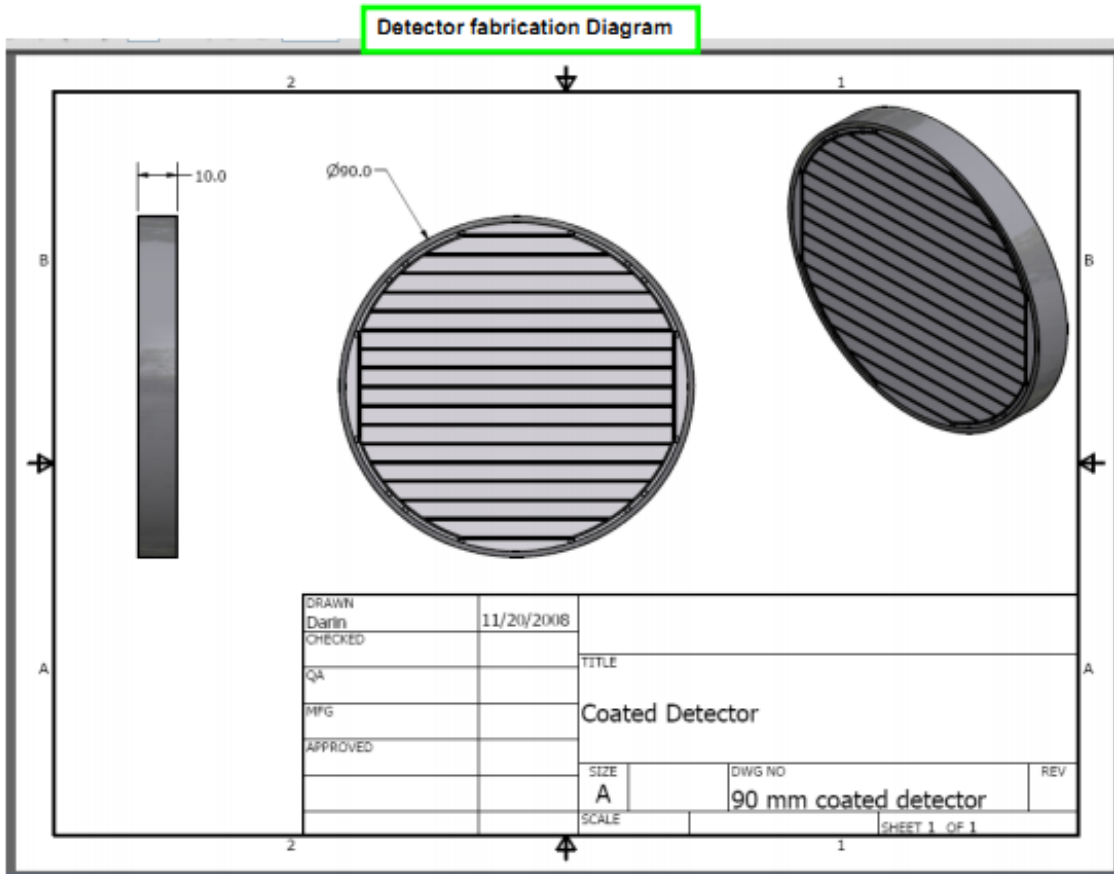


Figure 2.9: Side View of HPGe Strip Detector [23]

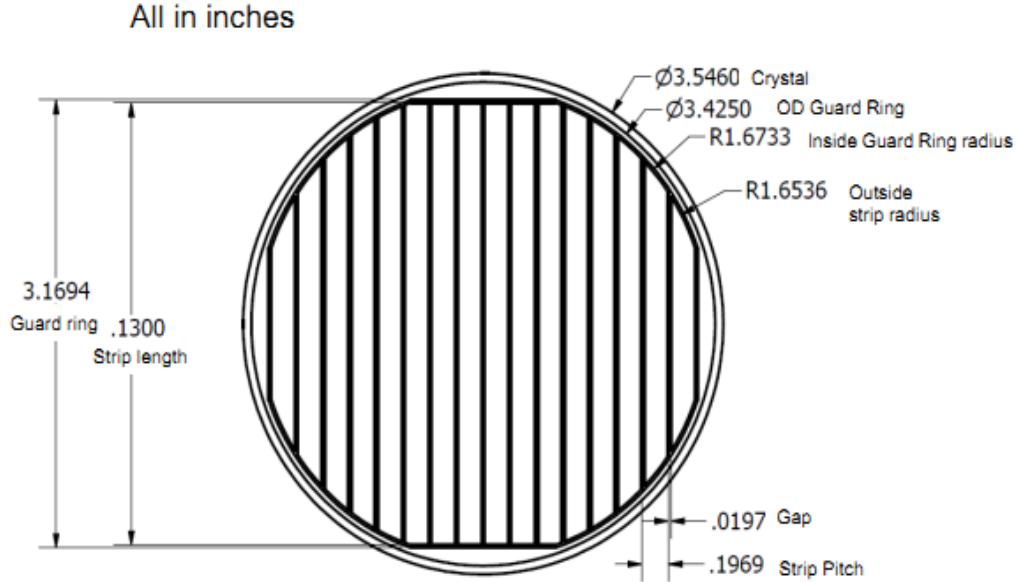


Figure 2.10: Front View of Detector [23]

The dimensions of the strips and crystal give enough information for three-dimensional positions of gamma ray interactions [17]. The primary application of having imaging capability is to detect a weak signal out of background radiation; imaging properties give spatial resolution which can distribute background measurements across the solid angle but still looking at the flux in one point [17]. They can operate with low count rates and high bandwidth which requires less energy to power the detector. With less power, it means the detector can be more compact and require less complicated cooling, thus making it more portable [17]. Unfortunately, these kinds of detectors need many channels to record gamma ray interactions on an individual basis [17].

2.4 Detector Dimensions and Setup

Oak Ridge National Laboratory (ORNL) supplied dimensions and detector setup. The actual detector setup is shown in Figures 2.11 and 2.12. The detector itself was manufactured by PHDs Co.

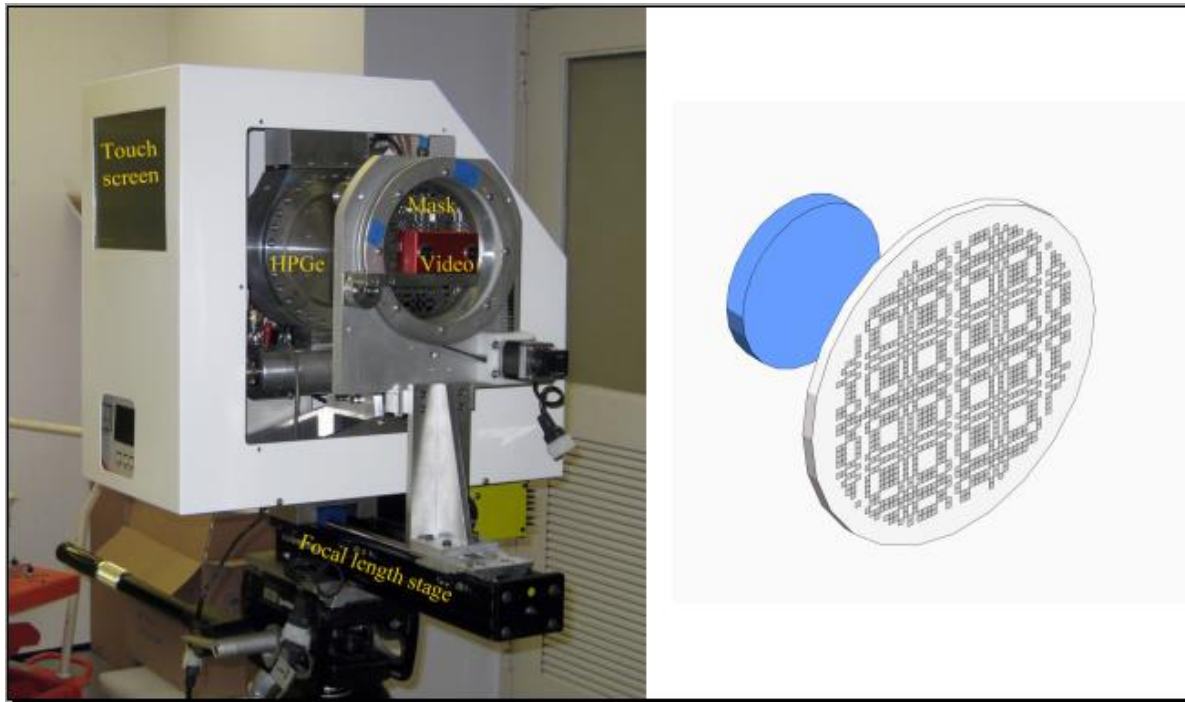


Figure 2.11: Detector Setup [23]

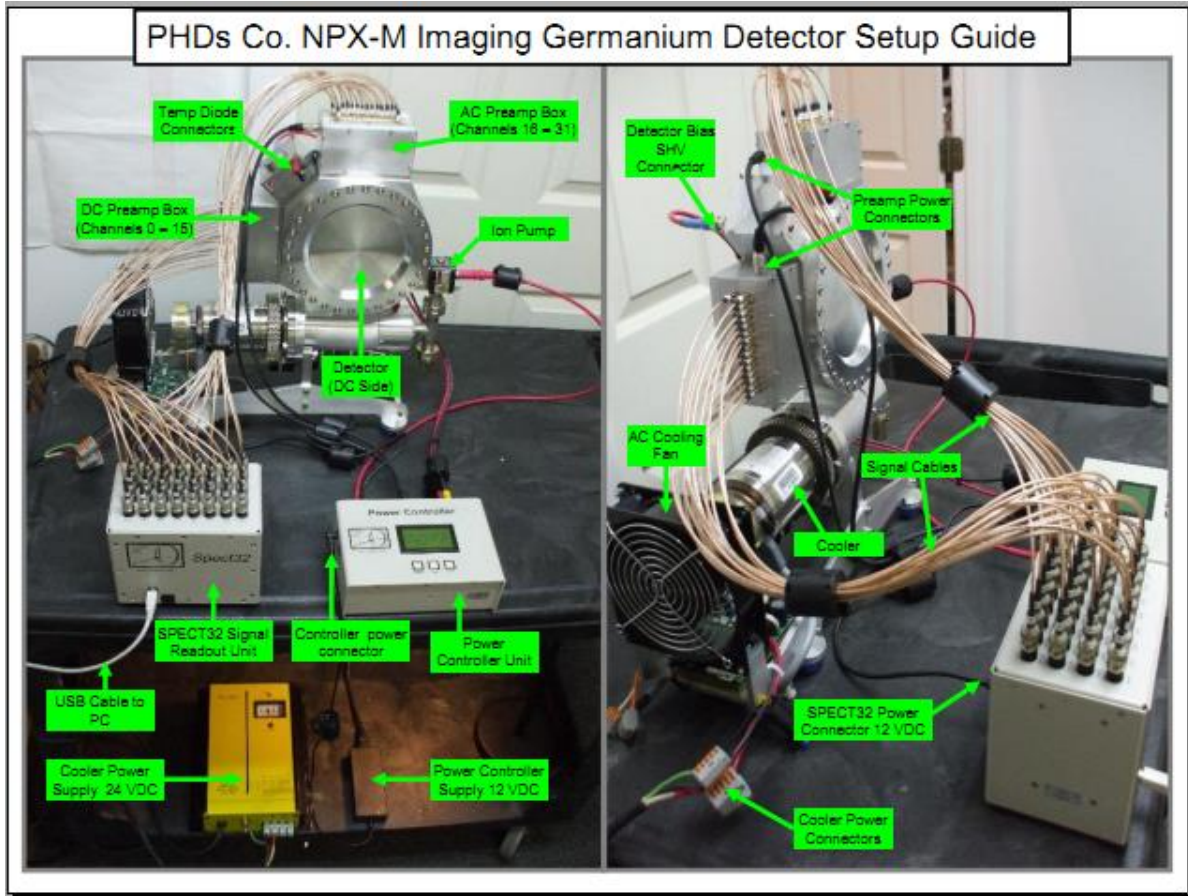


Figure 2.12: Detector Setup Continued. [23]

The conductive material on the strips making an anode is very thin. This was therefore neglected in the model. In addition, the detector electronics and casing were not included in the model since this information was proprietary and of negligible impact in the detection process.

2.5 Detector Response Functions

The Detector Response Function (DRF) is an inherent property of detectors that can be used to create a spectral library dependent on position and energy for a spectroscopic imager like the one described in the preceding section. It is defined by Equation 14.

$$S(E) = \int dE' R(E, E') Q(E') \quad (14)$$

E is the registered energy deposition, E' is the energy of the gamma ray emerging from the source, $S(E)$ is the detector spectrum, $R(E, E')$ is the response function, and $Q(E')$ is the source spectrum [15]. The discrete version used in this project takes on the form below (Equation 15).

$$S(E_n) = \sum_{m=1}^M \Delta E'_m R(E_n, E'_m) Q(E'_m) \quad (15)$$

Or, in matrix form:

$$\begin{pmatrix} S_1 \\ S_2 \\ S_3 \\ S_4 \\ \cdot \\ \cdot \\ \cdot \end{pmatrix} = \begin{pmatrix} R_{11} & R_{12} & R_{13} & R_{14} & \dots \\ R_{21} & R_{22} & R_{23} & R_{24} & \dots \\ \cdot & & & & \\ \cdot & & & & \\ \cdot & & & & \end{pmatrix} \begin{pmatrix} Q_1 \\ Q_2 \\ Q_3 \\ Q_4 \\ \cdot \\ \cdot \\ \cdot \end{pmatrix} \quad (16)$$

The DRF can be considered as relating the pulse height distribution to the emission spectrum of the source. These can be pre-calculated to save gamma-ray tracking time inside the detector [20]. All particles for a mono-energetic source spectrum start at the same energy but have a probability of depositing different energy inside the detector which is called a response function, $R(E, E')$. An example is shown below.

$$\begin{aligned} S(E) &= \int dE' R(E, E') \delta(E' - E_0) \\ S(E) &= R(E, E_0) \end{aligned} \tag{17}$$

Therefore, the detector system is defined by probability that a particle will deposit energy between E and $E+dE$ where energy E' is the source energy ($R(E, E')dE$) [21]. An example of a germanium DRF is seen in Figure 2.13.

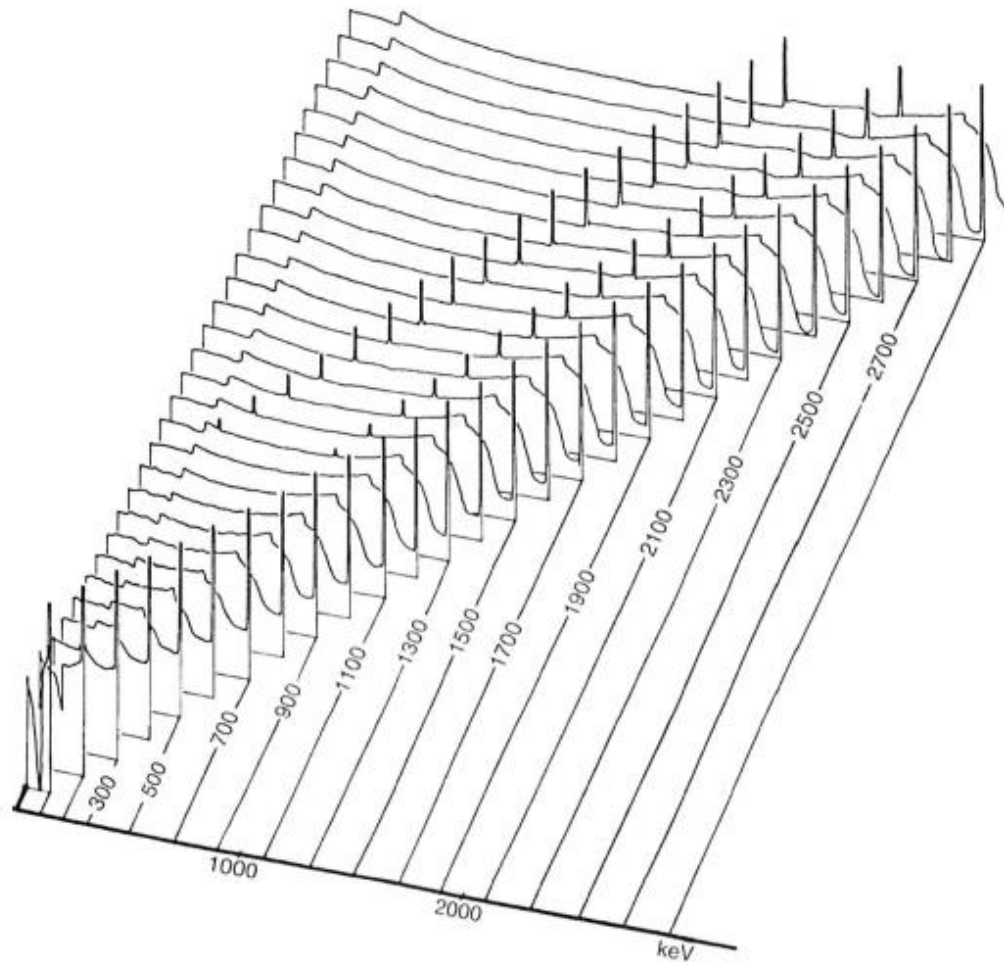


Figure 2.13: Germanium Detector Response Function Example [15]

Chapter 3: Procedures for Calculating the Detector Response Function

3.1 MCNPX-PoliMi Simulations

A computer model of the detector was created. The software used to build the model was Monte Carlo N-Particle (MCNPX) code for calculating photon transport. The specific version used was MCNPX PoliMi for its ability to log event-by-event photon interaction data, including each collision in the detector for each particle [39]. Important detector dimensions are given in Table 3.1 for the detector model.

Table 3.1: Important Detector Dimensions in MCNPX-PoliMi

<u>Detector Radius (cm)</u>	<u>Detector Thickness (cm)</u>	<u>Strip Gap (cm)</u>	<u>Strip Width (cm)</u>	<u>Source to Detector (cm)</u>
4.5034	1	0.025	0.45	30

The front and back views of the detector are shown in Figure 3.1 and Figure 3.2. Note that in Figure 3.2 that the hexagon shape is due to an approximation of a circle in the program, and is circular in this project as seen in Figure 3.1.

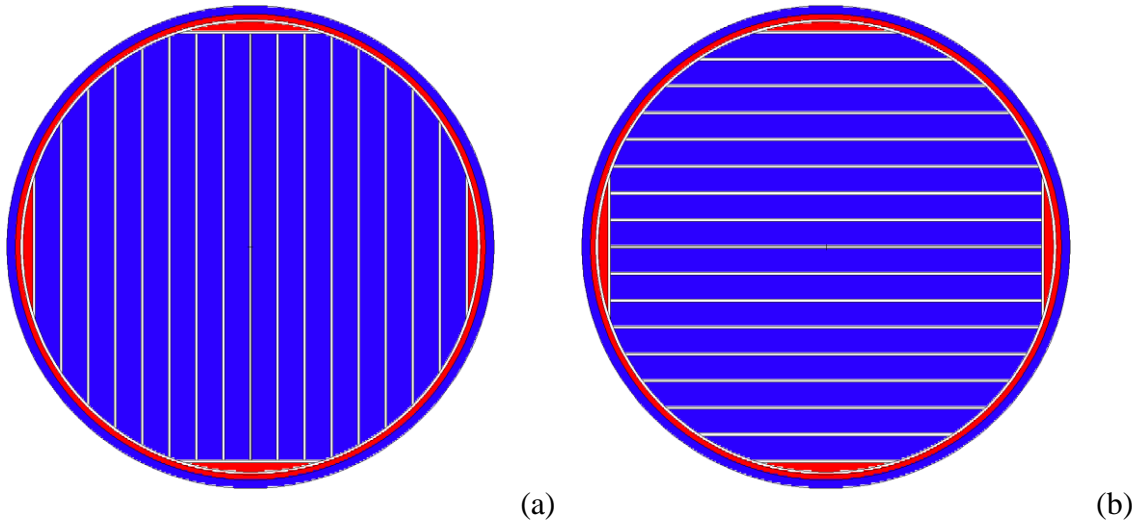


Figure 3.1: Front (a) and Back (b) Detector Views

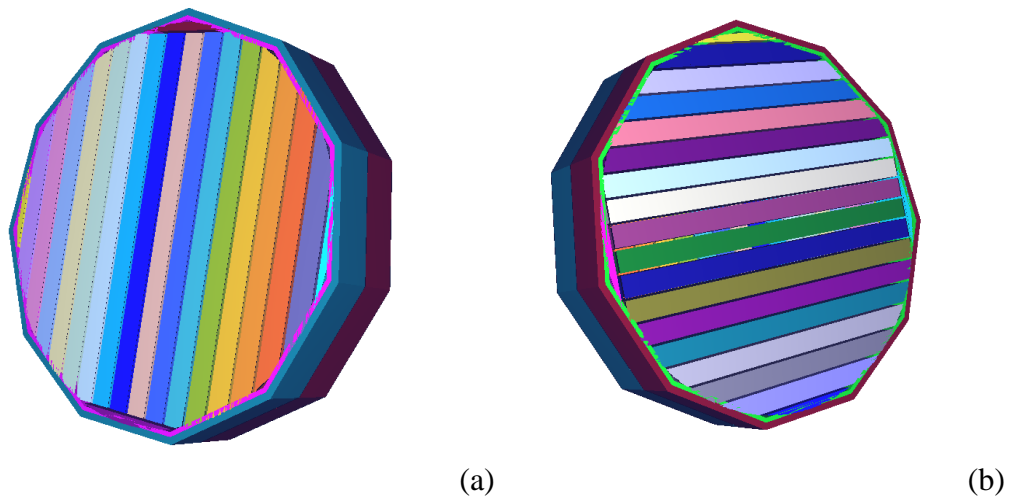


Figure 3.2: Front (a) and Back (b) Tilted Detector Views

To ensure that the detector model geometry was correct and exhibited our expectations for count distributions, one billion particles were run with a 200 keV point source, 30 cm away

from the detector. The point source was collimated into a cone of directions on the Z-axis. The conical angle was determined by the cosine relative the vector (VEC) described in the source card (the vector from the point source to the middle of the detector parallel to the Z-axis). The conical angle was first calculated to cover the entirety of the detector so the number of counts is maximized during a MCNPX-PoliMi run. In other words, all the particles are guaranteed to strike the detector.

The HPGe detector is double-sided, i.e. the electrode strips on the back are perpendicular to those on the front create a grid pattern in the strips. To model this, the front detector was rotated 90 degrees using a transformation card and placed 1 cm behind the front detector. The detector only processes a particle if its charge is collected by both the front and back electrode strips so it has enough spatial information to identify the (x,y) position of the interaction. The material used in this model was germanium for the detecting strips and non-sensing germanium for the guard rings of the detector. All guard rings and casing parts were non-sensing. Figure 3.3 shows the detector/source setup.

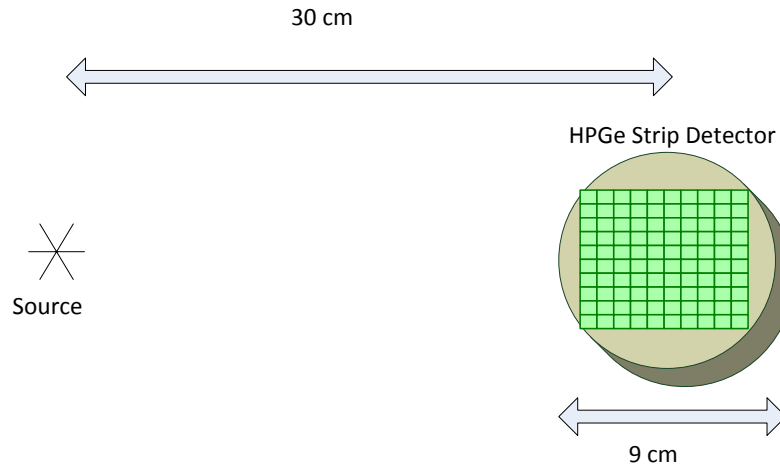


Figure 3.3: Detector/Source Setup

3.2 Creating Detector Image

To visualize the detector image and confirm MCNPX-PoliMi is correctly modeling the detector, a Python script was written to create an image from the log of photon interactions in the detector after each run as an image file (Figure 3.5). The Python script also generates a list of channel and energy number to be used in post-processing. More information about this list part of the algorithm will be described in the post-processing section (Section 3.5).

To create the detector image, the user specifies the number of pixels (320), the maximum energy to be observed (0.51 MeV), and the channel width (0.05 MeV). The object created in the Python script is made up of an array of pixels initialized to zero counts. The energy bins are arranged from zero to the maximum energy with the widths specified. Therefore, a “data cube” of the detector image is filled out in the grid containing the number of pixels in the x direction, the number of pixels in the y direction, and the number of counts

in each channel or energy bin. The depth of the voxels is in the z-direction, which is 1.0 cm.

To populate the grid, the position of the gamma ray interactions in the detector must be tracked. The MCNPX PoliMi log file, shown below (Figure 3.4), shows the energy deposited and outputs the x, y, and z coordinates in columns 8, 9, and 10, respectively, for each gamma ray interaction (particle history number).

Table 1
MCNP-PoliMi output file: excerpt

History number	Particle number	Projectile type ^a	Interaction type ^b	Target nucleus ^c	Cell number	Energy deposited (MeV)	Time (shakes)	Collision position (x,y,z)			WGT	Generation number	Number scatterings	Code
16	97	1	-99	1001	2	0.5309	8.095	43.57	4.88	1.84	1	3	5	0
16	97	1	-99	1001	2	0.0553	8.395	44.29	5.57	1.85	1	3	6	0
16	97	1	-99	1001	2	0.0014	11.722	44.92	5.04	3.78	1	3	9	0
109	1	1	0	6000	5	8.398	1.798	43.98	-7.52	6.31	1	0	0	0
132	1	1	-99	1001	5	13.9313	1.778	42.06	-2.98	1.42	1	0	2	0
132	1	1	-99	1001	5	0.1036	2.075	42.55	-2.34	2.88	1	0	3	0
132	1	1	-99	1001	5	0.0281	2.264	42.25	-2.39	3.44	1	0	4	0
132	1	1	-99	1001	5	0.0131	2.372	42.16	-2.22	3.63	1	0	5	0
335	58	1	-99	6000	4	0.0019	3.72	43.98	0.16	9.54	1	3	5	0
335	58	1	-99	1001	3	0.0042	4.069	42.64	-0.01	9.13	1	3	6	0
485	1	1	-99	1001	5	8.2582	1.872	48.08	-2.19	7.51	1	0	1	0
495	24	2	1	6	2	0.1461	1.036	43.87	3.46	5.06	1	1	2	0
495	24	2	1	6	2	1.2823	1.036	43.95	3.47	5.08	1	1	3	-1
495	24	2	1	6	2	0.038	1.038	43.41	3.8	5.12	1	1	4	-1
495	24	2	1	1	2	0.0793	1.038	43.28	3.76	5.08	1	1	5	-1
495	24	2	1	6	2	0.0421	1.042	43.69	3.19	5.93	1	1	6	-1

^a 1 = neutron; 2 = photon.

^b -99 = elastic scattering; 1 = Compton scattering; 0 = absorption.

^c 1001 and 1 = hydrogen; 6000 and 6 = carbon.

Figure 3.4:MCNPX PoliMi Log File Showing x,y, and z Coordinates and Energy Deposited [39]

The coordinates of the interactions from the log file are converted into pixel coordinates by halving the number (N) of pixels (to be at the center of the detector) and adding the x value coordinate (x) divided by 0.05 cm. This creates coordinates with the center at (0,0,0).

$$\frac{N}{2} + \frac{x}{.05} = \text{Pixel Position} \quad (18)$$

This is the physical smallest pixel. As previously mentioned in Chapter 2, the detector only counts particles that are registered by both the front and back electrodes, so the script only records gamma rays that strike sensitive germanium cells in both the front and back of the detector. To find the appropriate channel for the energies, each energy is divided by the maximum energy specified and multiplied times the channel width. The channel of each of these collisions is populated with the corresponding pixel.

The Python script uses matplotlib to plot the energy and collisions in pixels of the detector. Figure 3.5 shows the detector (intensity on each pixel) after running 10^9 particles. A clear grid pattern is seen from the germanium strips while the non-sensing germanium parts of the detector are not apparent, as expected.

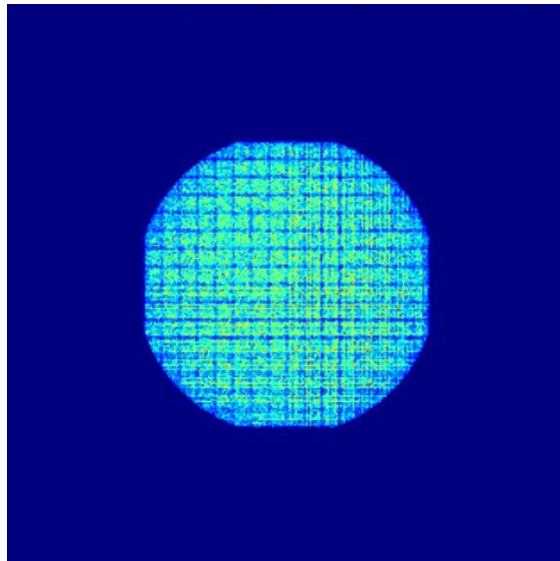


Figure 3.5: HPGe Strip Detector Image Running 10^9 Particles

3.3 Determining Source Beam Radius

To calculate the detector response function, the best source beam width must be determined. Without this calculation, the number of histories for each run would be enormous, since there are 50 channels by 40 source energies by 160 pixels by 160 pixels- too much data to handle efficiently. The optimal beam width would be the number of counts in a physical pixel where increasing beam width no longer contributes to more counts in that pixel. The physical pixel is defined by the strips of the front and rotated detector which form a grid when overlapped. The size of one square in the grid is referred to as the physical pixel of the detector which is 0.45 cm x 0.45 cm (Figure 3.6). The detector face with a beam radius 2.75 cm to the left of the center with arbitrary source energy of 0.2886 MeV and one million particles is shown in Figure 3.7.

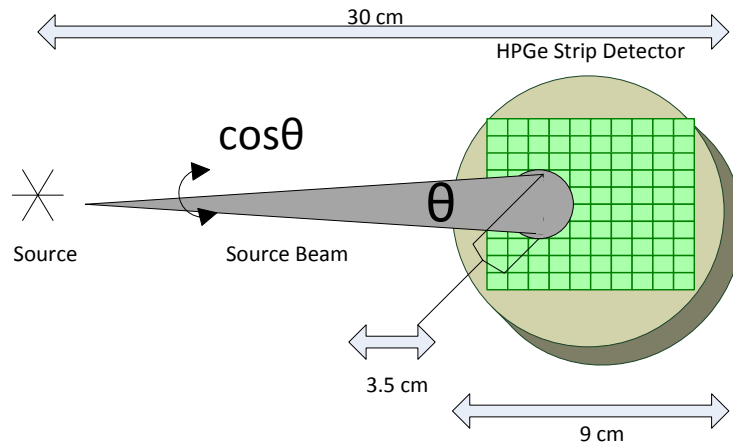


Figure 3.6: Setup for Determining Beam Width

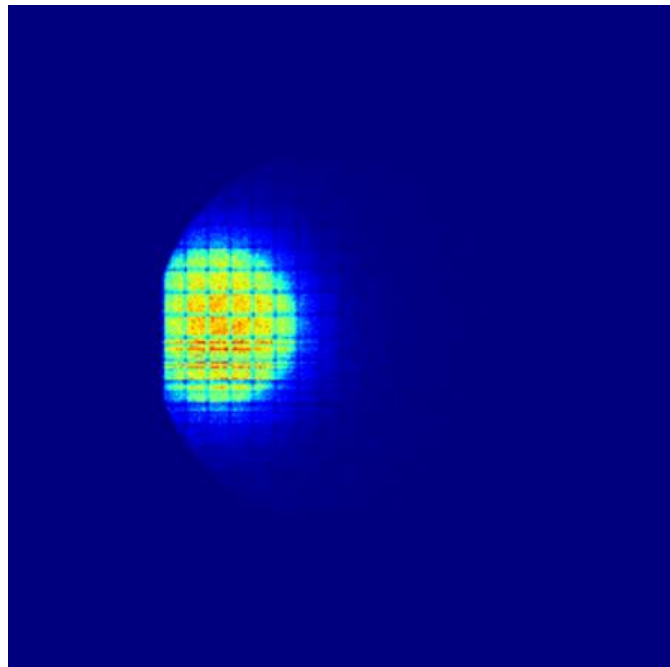


Figure 3.7: Detector Face Beam Width Visualization

The input deck used for the detector was modified in the source card to account for increasing source beam widths at 200 keV. The direction of the beam was also changed to reflect which pixel was being analyzed. The vector (VEC) from the source to the detector was shifted to point to each new pixel being analyzed which comes from the cosine of this vector. In addition, the conical angle determining the beam width by the cosine relative to the vector (VEC) was increased incrementally from a width of 0 to 90 mm. This was done for a physical pixel located in the center of the detector, a pixel at the far left of the detector, and a pixel at the very top of the detector, due to the symmetry of the detector. Results of the normalized subset counts are shown in Figures 3.8, 3.9, 3.10, respectively.

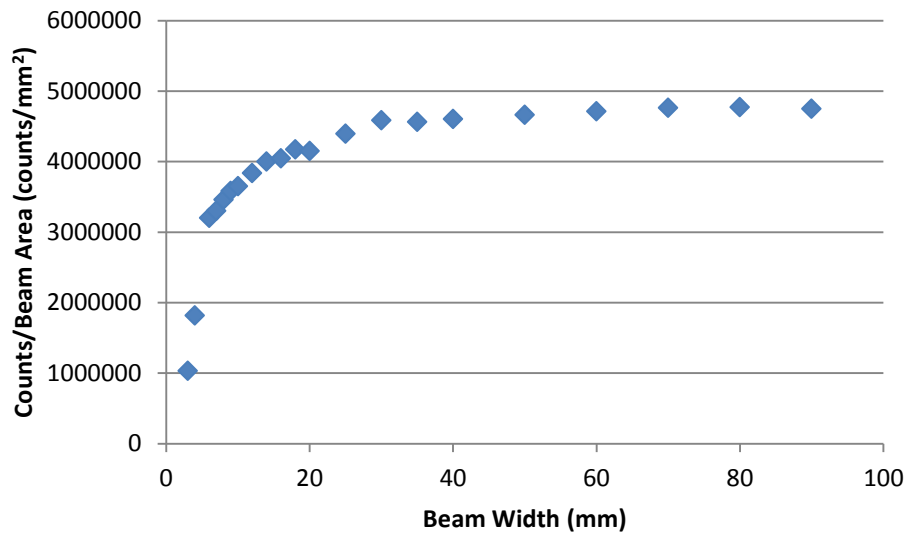


Figure 3.8: Center Pixel Counts vs. Source Beam Width

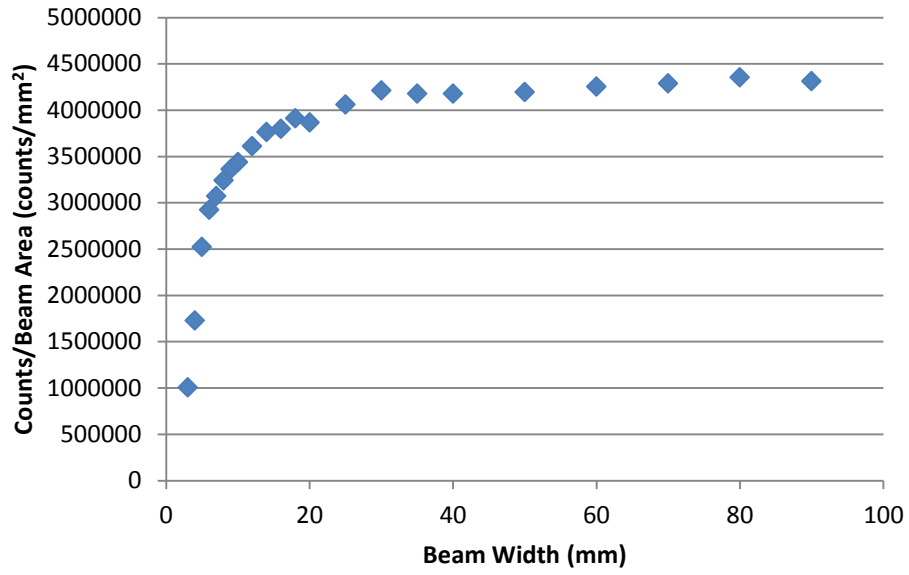


Figure 3.9: Far Left Pixel Subset Counts vs. Source Beam Width

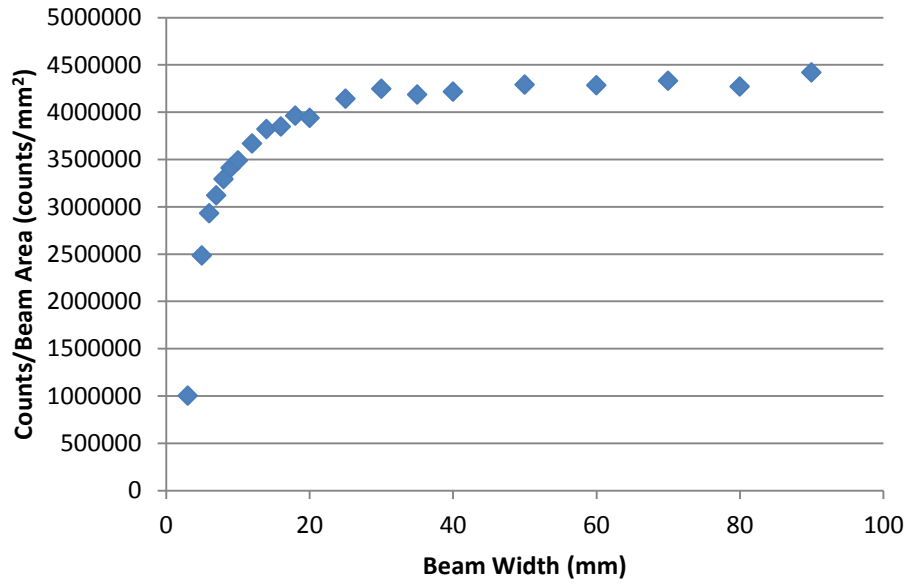


Figure 3.10: Top Pixel Subset Counts vs. Source Beam Width

Based on these figures, the appropriate beam spot size is about 35 mm for every pixel examined because this is where the counts stop changing significantly with increasing spot size. The number of counts in each physical pixel should approach an asymptotic value as the beam width increases because the photons contained in the width of the beam become more likely to hit outside of the pixel area where the beam is directed. However, the conical beam width sweeping the pixels will eventually increase enough to where the counts stop increasing in the physical pixel. The photons striking the detector at the edge of the beam rarely scatter into the pixel at the center of the beam. This ultimately improves the efficiency of the simulation.

3.4 Determining Energies to Run

To create the detector response function of this detector, energies must be chosen to represent the FWHM (Full Width Half Maximum) curve for a Germanium detector. The resolution of the detector can be modeled from the standard deviation of its Gaussian distribution, which is in a power-law form where σ is the standard deviation of the resolution, E is the gamma ray energy, and a and b are constants determined experimentally [22].

$$\sigma = aE^b \quad (19)$$

The FWHM is related by this standard deviation [22].

$$\text{FWHM}=2.35\sigma \quad (20)$$

Because this curve is represented by a power law function, some energies will be sampled closer together to get a more accurate representation of this Energy vs. FWHM curve. In other words, this refines the energy mesh to get a more accurate representation of the energy. Forty energies were selected and used in the MCNPX-PoliMi input deck for the reference spectra of the eventual detector response function (Figure 3.11).

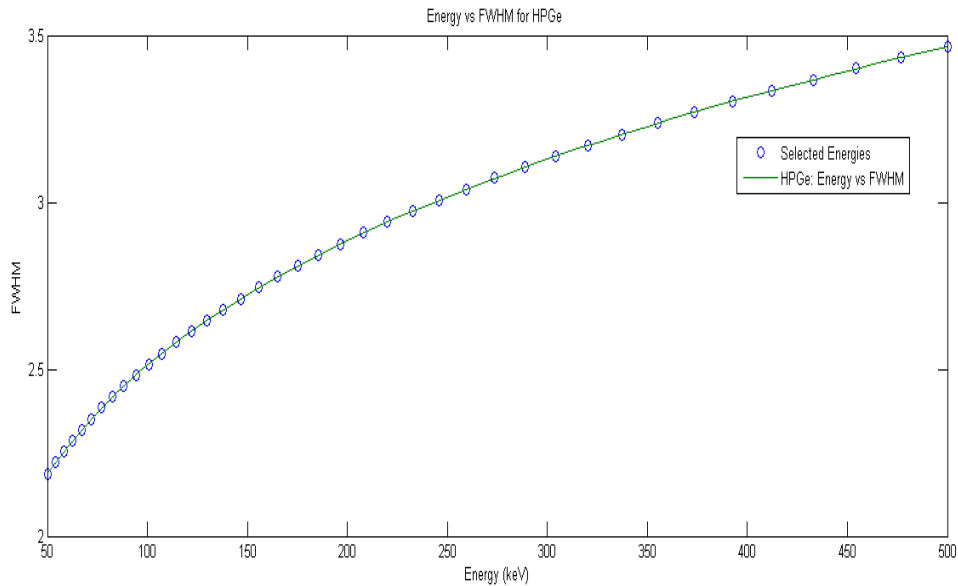


Figure 3.11: Energy vs FWHM for HPGe Detector

3.5 Creating Input Files and Running Script on 32 CPUs

To expedite running forty instances of MCNPX-PoliMi, input cards with an energy variable were created which allowed a python script to replace this variable with a specific

energy (Figure 3.11) and run the MCNPX-PoliMi instance across 31 CPUs (Figure 3.12). This dramatically reduces the effort and time required to collect these data.

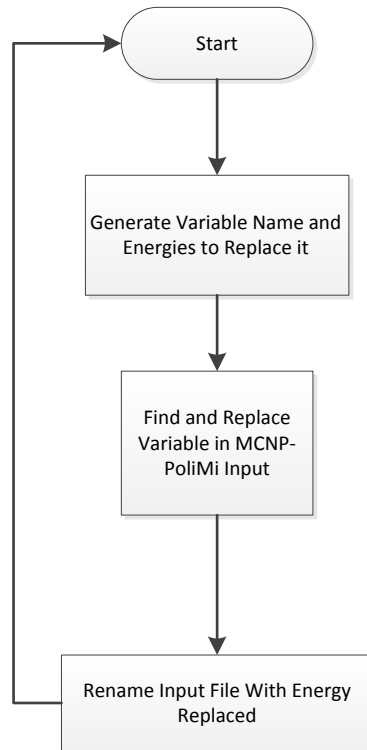


Figure 3.12: Input Card Generating Algorithm

The algorithm for running all these instances of MCNPX-PoliMi defines the number of cores and renames the outputs and log files with the corresponding input name. With this information, the MCNPX-PoliMi run commands can be created and run across multiple cores with the appropriate naming conventions to organize the data (Figure 3.13).

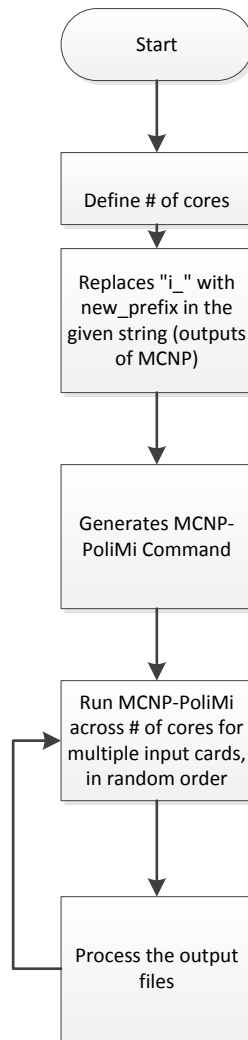


Figure 3.13: Algorithm for running instances of MCNPX-PoliMi across N CPUs

3.6 Proving Radial Symmetry of the Detector

By using the 35 mm beam width, the count distribution across the detector was established. Starting at the center and shifting the beam direction in 50 mm increments across the entire detector face, the count distribution was analyzed (Figure 3.14, 3.15). The counts drop off because of the non-detecting regions on the boundary.

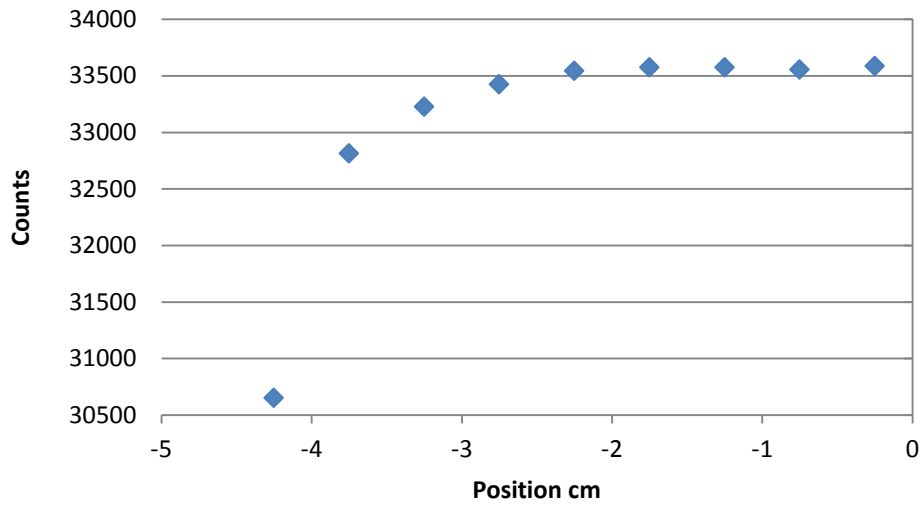


Figure 3.14: Distribution of Pixel Counts in the Y Direction

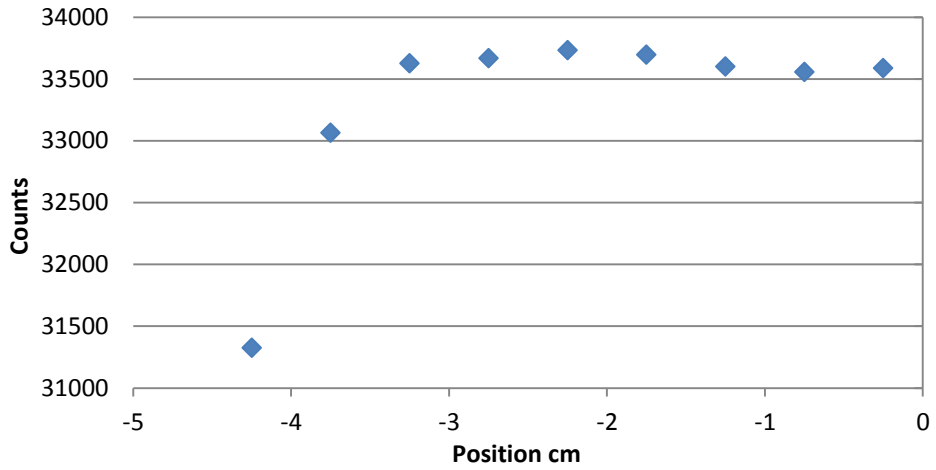


Figure 3.15: Distribution of Pixel Counts in X Direction

Table 3.2: Count Error for Comparing X and Y Directions

<u>Beam Distance from Center Point (cm)</u>	<u>Difference in X and Y Counts</u>	<u>Percent Difference</u>	<u>Std Dev Y Direction</u>	<u>Std Dev X Direction</u>
0	0	0	1160	1160
0.25	0	0	1161	1161
0.75	456	0.033	1160	1160
1.25	651	0.048	1159	1159
1.75	2157	0.165	1156	1155
2.25	1887	0.144	1145	1144
2.75	1328	0.123	1086	1086
3.25	816	0.083	987	988
3.75	1047	0.128	903	902
4.25	2242	0.431	721	723

From Table 3.2, the percent difference between the x and y directions never reach 0.5%. This allows the assumption that the x and y directions may be treated as a single radial dimension.

Figure 3.16 shows how the spectrum changes in the x direction with changing beam distances from the center. As the beam is directed at an area farther from the center of the detector, counts are lost by gamma rays escaping the boundary of the detector. Therefore, as expected, the center point has the most counts and 4.25 cm from the center has the least number of counts.

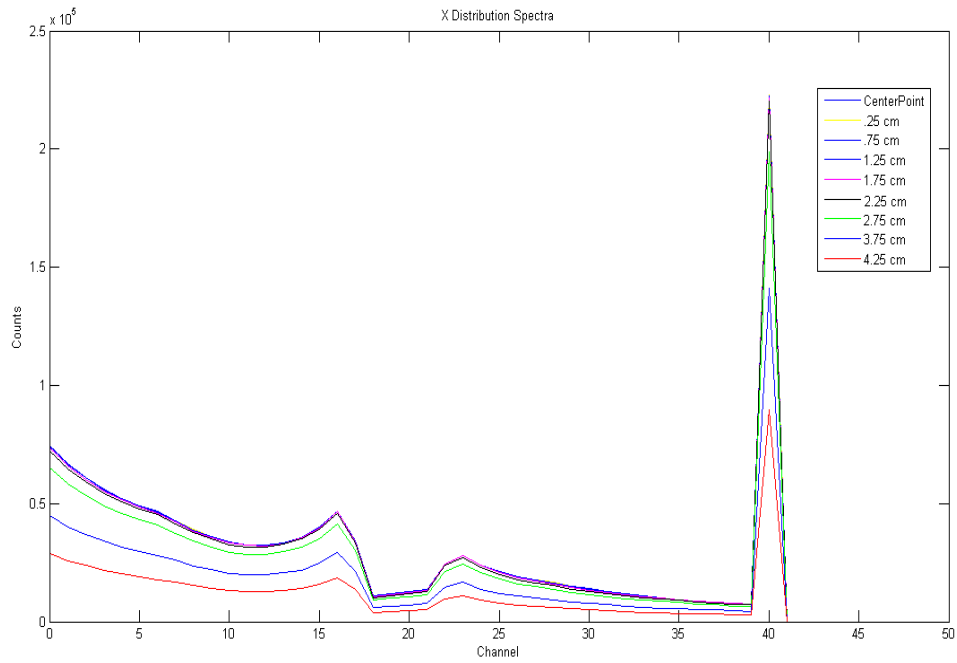


Figure 3.16: Spectral Changes with X-Position

Similarly, results were seen in the y direction (Figure 3.17)

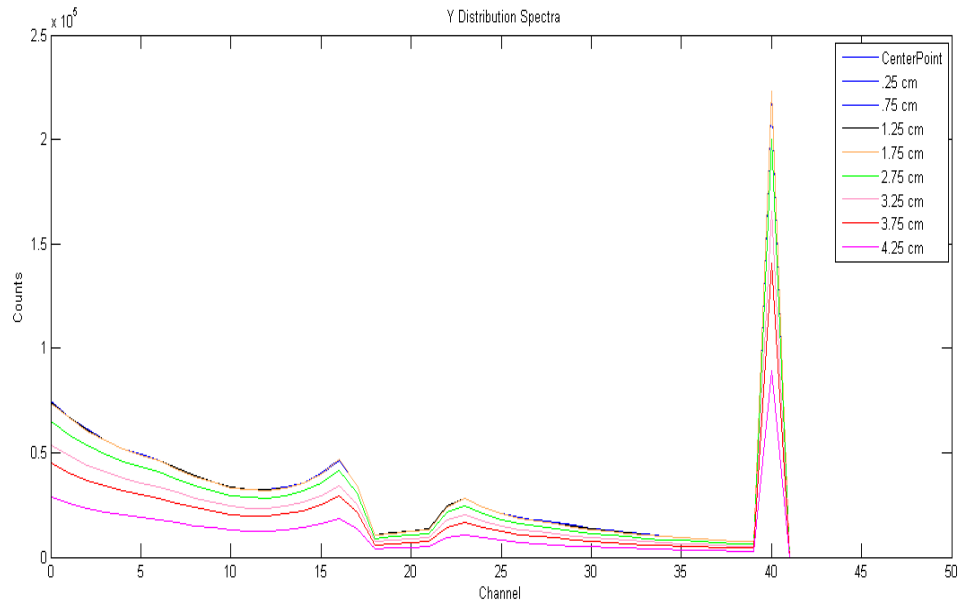


Figure 3.17: Spectral Changes with Y-Position

To further prove the radial symmetry of the detector, spectra from the x and y directions were interpolated to find the spectrum expected at a point between these two directions. Conventional bilinear interpolation does not work in this case because we are interpolating on a circular surface.

A method called SLERP, or Spherical Linear Interpolation, essentially takes two vectors (the spectra in the x and y directions) and interpolates the rotation about these vectors. The shortest path on this unit sphere can be scaled to the right magnitudes [11]. This was implemented in a script in MATLAB (Figure 3.18, 3.19) [12].

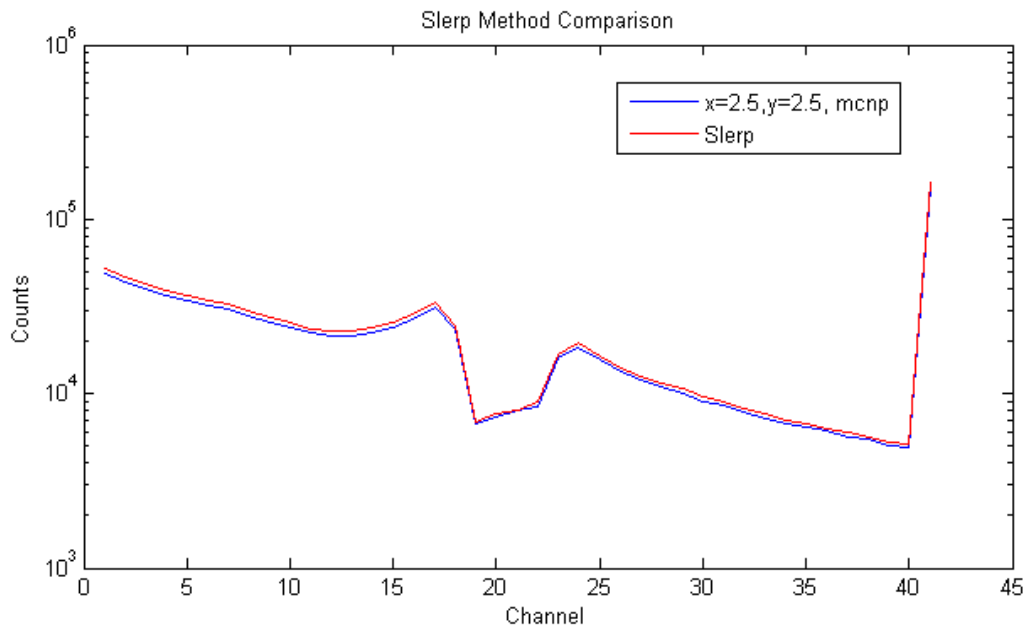


Figure 3.18: Log Scale Comparing SLERP Method and MCNPX-PoliMi Direct Calculation

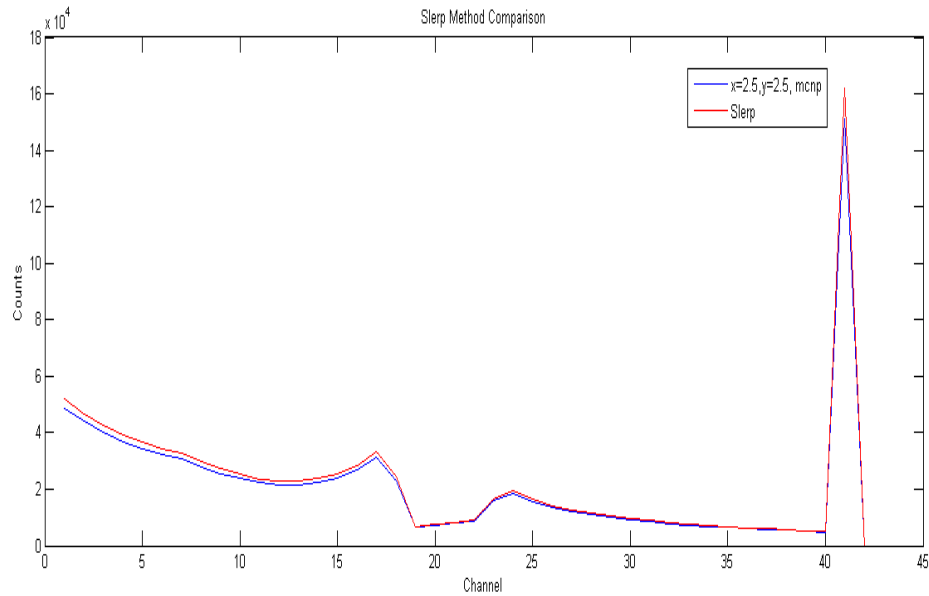


Figure 3.19: Linear Scale Comparing SLERP Method and MCNPX-PoliMi Direct Calculation

These two figures show that the detector is radially symmetric because the SLERP values coincide with MCNPX-PoliMi generated spectra in addition to the x and y directions previously shown in Figures 3.16 and 3.17.

3.7 Interpolating Separate Features of the Spectrum

The MCNPX-PoliMi generated spectrum must be split into separate features based on different photon interactions before the spectrum can be interpolated. Some features of gamma spectra do not change linearly when the source energy is changed and therefore cannot be extrapolated for the entire spectrum. The python algorithm to extract the features is

show in Figure 3.20. The algorithm uses all the log files generated from the MCNPX-PoliMi runs shown previously in Figure 3.12 and Figure 3.13.

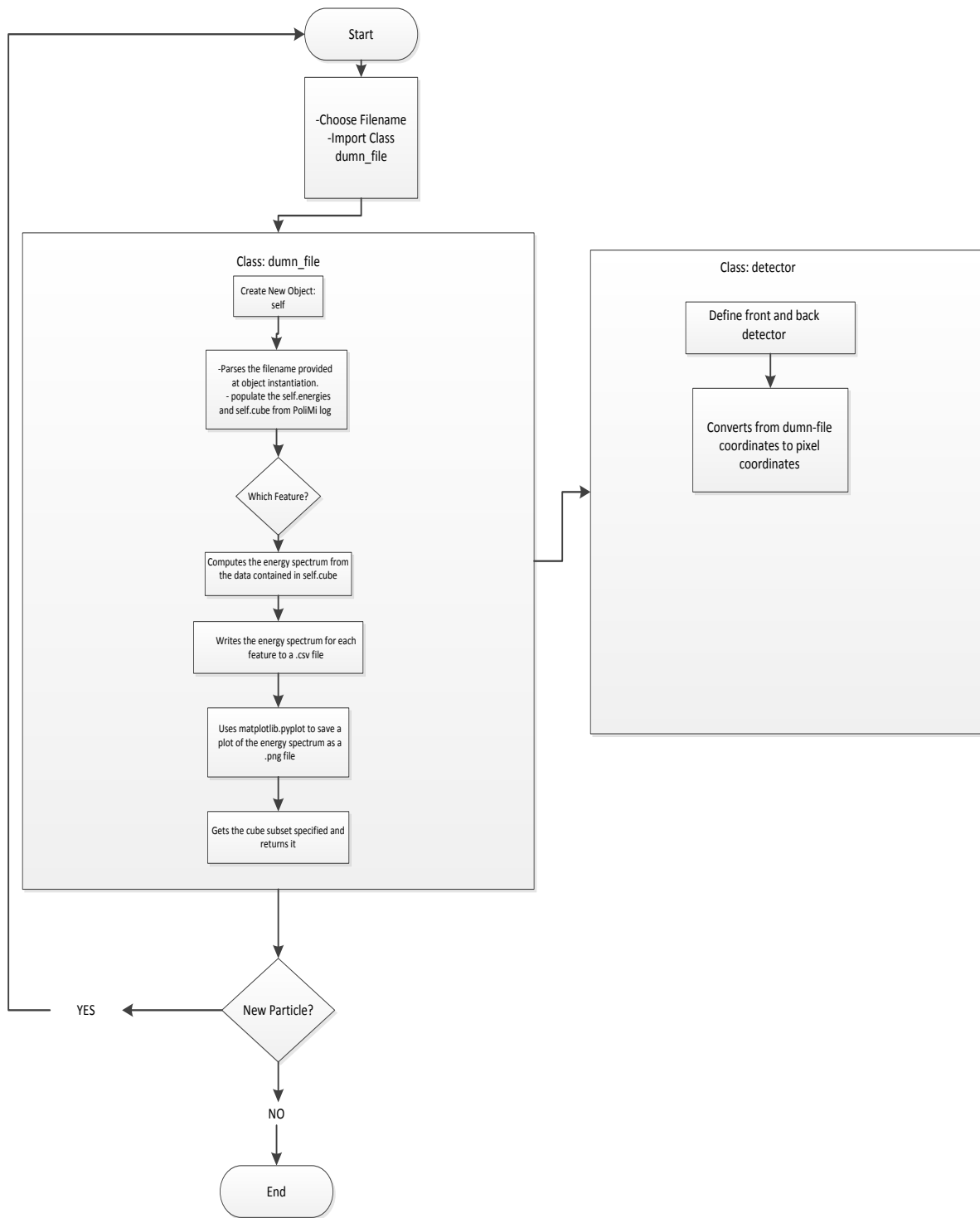


Figure 3.20: Detector Response Function Data Building Algorithm

The log files appear in the form of Figure 3.21. As mentioned before, this algorithm also produces an image file that shows the detector face displaying where the most collisions happened. The data columns used in this post-processing include: particle history number, interaction type, cell number of collision event, collision position, and number of scatterings. This information is extracted and put into one of three spectral feature categories: Compton scattering, full energy peak, and the backscatter peak. These were saved as a list for use in Matlab to be interpolated.

Table 1
MCNP-PoliMi output file: excerpt

History number	Particle number	Projectile type ^a	Interaction type ^b	Target nucleus ^c	Cell number	Energy deposited (MeV)	Time (shakes)	Collision position (x,y,z)			WGT	Generation number	Number scatterings	Code
—	—	—	—	—	—	—	—	—	—	—	—	—	—	—
16	97	1	-99	1001	2	0.5309	8.095	43.57	4.88	1.84	1	3	5	0
16	97	1	-99	1001	2	0.0553	8.395	44.29	5.57	1.85	1	3	6	0
16	97	1	-99	1001	2	0.0014	11.722	44.92	5.04	3.78	1	3	9	0
109	1	1	0	6000	5	8.398	1.798	43.98	-7.52	6.31	1	0	0	0
132	1	1	-99	1001	5	13.9313	1.778	42.06	-2.98	1.42	1	0	2	0
132	1	1	-99	1001	5	0.1036	2.075	42.55	-2.34	2.88	1	0	3	0
132	1	1	-99	1001	5	0.0281	2.264	42.25	-2.39	3.44	1	0	4	0
132	1	1	-99	1001	5	0.0131	2.372	42.16	-2.22	3.63	1	0	5	0
335	58	1	-99	6000	4	0.0019	3.72	43.98	0.16	9.54	1	3	5	0
335	58	1	-99	1001	3	0.0042	4.069	42.64	-0.01	9.13	1	3	6	0
485	1	1	-99	1001	5	8.2582	1.872	48.08	-2.19	7.51	1	0	1	0
495	24	2	1	6	2	0.1461	1.036	43.87	3.46	5.06	1	1	2	0
495	24	2	1	6	2	1.2823	1.036	43.95	3.47	5.08	1	1	3	-1
495	24	2	1	6	2	0.038	1.038	43.41	3.8	5.12	1	1	4	-1
495	24	2	1	1	2	0.0793	1.038	43.28	3.76	5.08	1	1	5	-1
495	24	2	1	6	2	0.0421	1.042	43.69	3.19	5.93	1	1	6	-1

^a 1 = neutron; 2 = photon.

^b -99 = elastic scattering; 1 = Compton scattering; 0 = absorption.

^c 1001 and 1 = hydrogen; 6000 and 6 = carbon.

Figure 3.21: MCNPX-PoliMi Output File Log [39]

To determine which feature each particle belongs to (backscatter, Compton, or full energy peak), a simple algorithm was used (Figure 3.22). As stated in Chapter 2, a particle

must collide in both the front and back parts of the detector to register a collision. When this happens, the particle interaction type on the last collision, either an absorption or scatter (0 or 1), is noted. When it ends in a scatter event (1), it is a Compton feature. If it ends in absorption, then this particle belongs to the full energy peak or backscatter category. To determine which feature it belongs to, the value in the collision column is checked to determine if it is monotonically increasing. If it is, this means all collisions occurred in the sensing cells of the detector which makes it part of the full energy peak. If instead there is a missing collision, then the particle had an interaction outside the sensing cells of the detector but then scattered back into a sensing cell of the detector making it a backscatter feature.

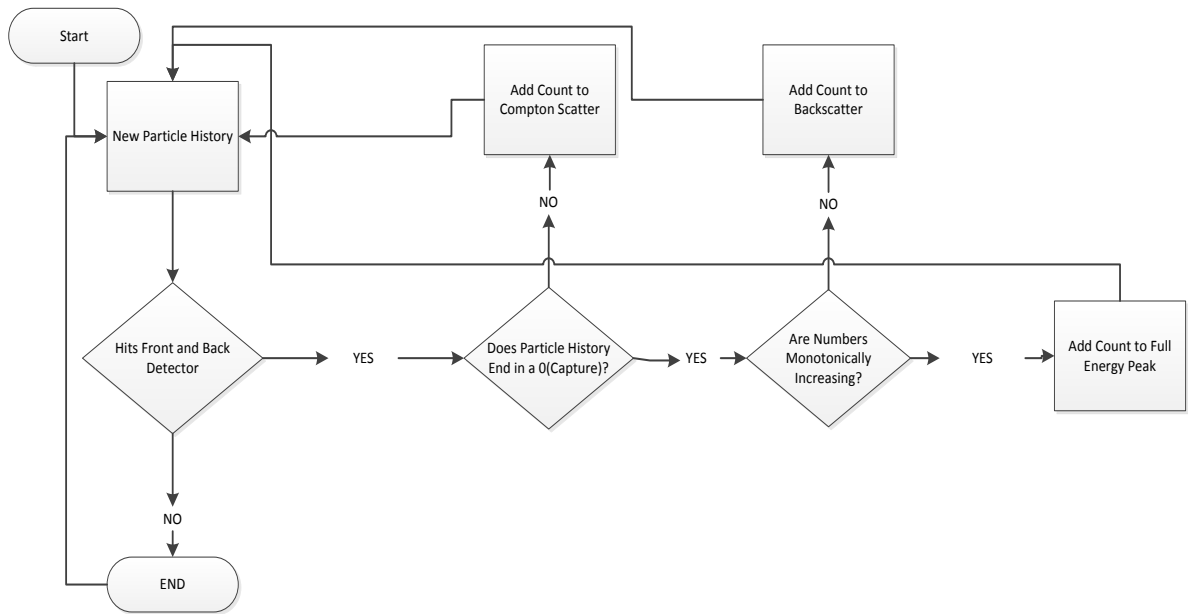


Figure 3.22: Algorithm for Determining Feature from Particle History

To interpolate each feature, the list files were loaded into MATLAB. The full energy peak, backscatter, and Compton scattering were interpolated. First, the radial positions and energies calculated are tabulated in a large array. The user inputs the desired radial position and energy in the detector and MATLAB accesses the corrected lower and upper position and energy spectra.

The x-coordinate for the interpolated full energy peak is the source energy. The ratio of this energy to the x-coordinate of either the upper or lower spectrum full energy peak was calculated. This number was used to multiply the entire upper or lower spectrum abscissa (energy) values to yield a new interpolated spectrum.

To find the interpolated ordinate values (counts) of the spectrum, the line between the upper and lower peaks is calculated using Equation 21 and shown in Figure 3.23.

$$y = mx + b \quad (21)$$

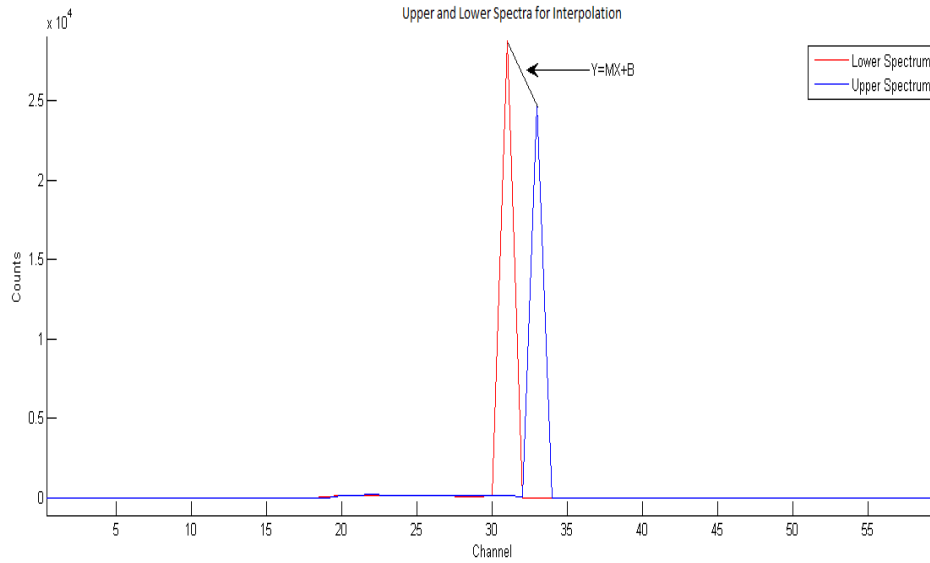


Figure 3.23: Determining Interpolation Counts from Lower and Upper Spectra

Because two points on the line are known (the two peaks), the slope m for each feature can be directly calculated using Equation 22 for the 3 separate features (full energy peak, Compton edge/continuum, and backscatter peak).

$$m = \frac{y_1 - y_2}{x_1 - x_2} \quad (22)$$

The point-slope version was used, Equation 23, where m is the slope and (x_1, y_1) is the upper or lower spectrum peak and x is the known location of the full energy peak which in this case is merely the source energy. The number of counts in the peak of the interpolated spectrum (y) can now be calculated [33].

$$y - y_1 = m(x - x_1) \quad (23)$$

From this, a ratio was found by dividing this y value by the y value of the counts at the peak of either the lower or upper spectrum. This number is multiplied by all the y-values on the newly x-interpolated spectrum from above. The interpolated spectrum is now defined.

This interpolation method was used for the backscatter and Compton scattering features [33]. However, the location of the x-coordinate for the interpolated spectrum is different for both of these features. For Compton scattering, Equation 5 is used and for backscatter Equation 6 is used from Chapter 2. As a result of the new position, the continuum is stretched to fit the new x-values.

$$T_{e-,max} = E_\gamma - E'_{\gamma,min} \quad (5)$$

$$E'_\gamma = \frac{E_\gamma}{1 + \frac{2E_\gamma}{m_e c^2}} \quad (6)$$

Finally, the counts of the three spectra are summed to get the complete number of counts.

The average of the three spectra's x-values was used for the energies of these counts on the x-axis.

3.8 Re-binning Interpolated Energy Bins to MCNPX Energy Bins

In order to compare the interpolated spectra with the MCNPX PoliMi calculations, the interpolated energy bins must be re-binned into the original 50 keV interval energy bins. This allows the spectrum to be compared directly with the MCNPX-PoliMi calculated spectrum that uses the 50 keV binning structure.

To re-bin the interpolated data, a script in Haskell was used [24]. In short, this script takes advantage of the “sweep” style algorithm, which means it takes the x-coordinate data and “sweeps” from left to right to calculate how many counts are in each new energy bin. It creates a “number line” of each increasing bin and when they overlap, the counts are split based on a linear weight based on the amount of overlap of the two bins. To clarify, the contributions of each pixel are weighted.

To use this code, the user will input x_1 , y_1 , and x_2 which correspond to the interpolated spectrum x values (energy bins), the interpolated y values (counts), and the desired MCNPX-PoliMi based binning, respectively. The sweep style algorithm can determine the number of counts from the x_1 bins that go into the new x_2 bins based on how they line up on the bin number line, shown in Figure 3.24.

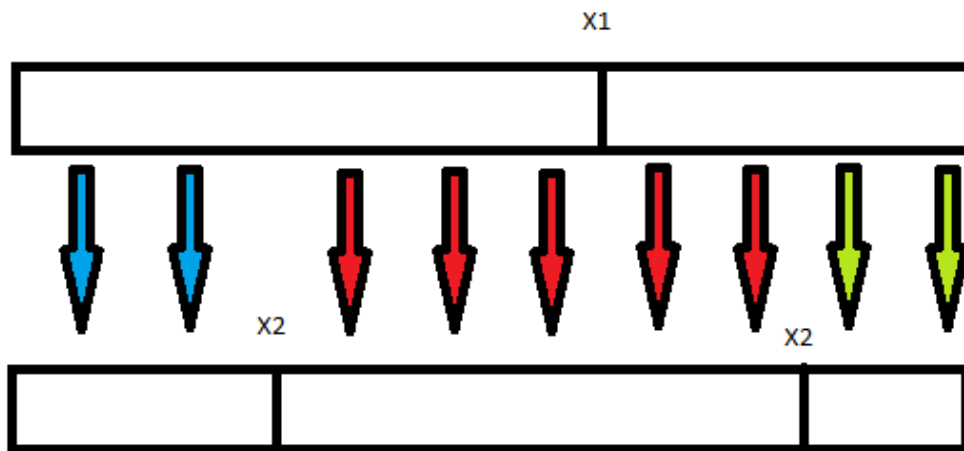


Figure 3.24: Sweep-Style Re-binning Algorithm for Interpolated Bins (X1) and the MCNPX-PoliMi Bins.

If x_2 comes before the next x_1 value, a fraction of the x_1 counts will go into the first x_2 bin while the remaining fraction goes into the following x_2 bin [25]. This assumes that the energies are uniformly distributed in the bins.

Chapter 4: Results

4.1 Calculated Response Function

The response function that the interpolated method draws from should be in the form of the figure in Chapter 2, Figure 2.11. This response function for the HPGGe detector is shown in Figure 4.1 and Figure 4.2 with a radius near the center of the detector.

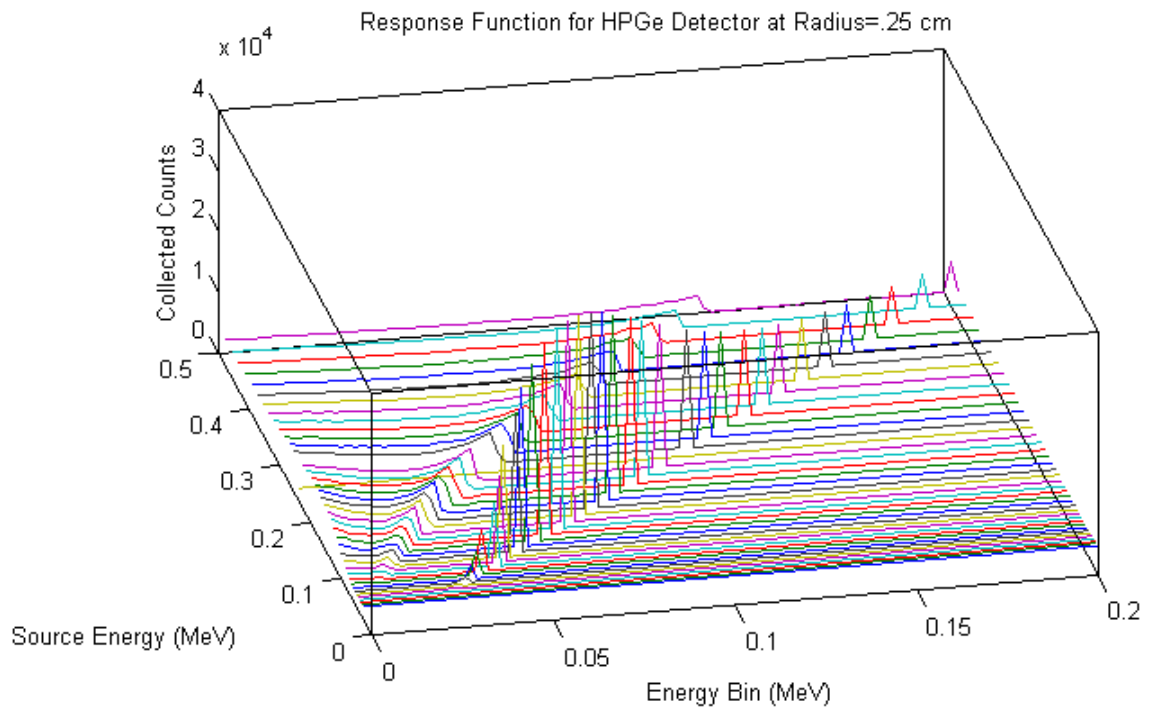


Figure 4.1: Response Function for the HPGe Strip detector at 0.25 cm Radius

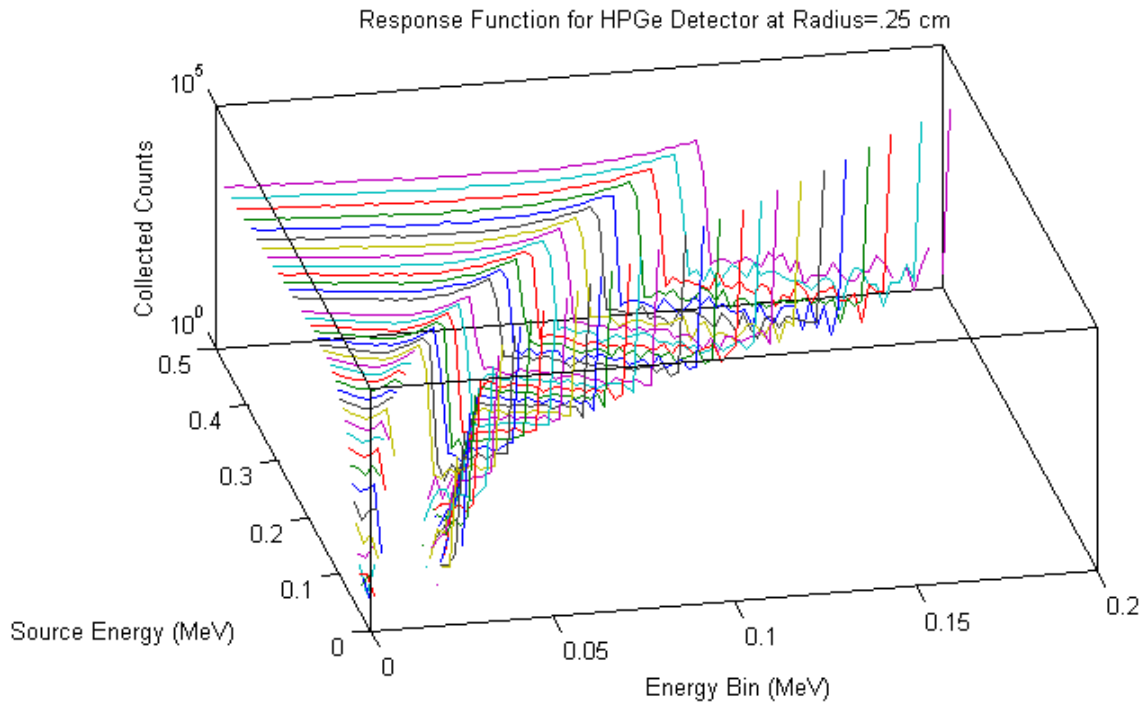


Figure 4.2: Response Function for the HPGe Strip detector at 0.25 cm Radius (Log Scale)

The plot follows a similar trend as the example with a full energy peak following the diagonal. Similarly, if a radius closer to the edge of the detector was chosen, a plot with fewer counts is expected. This is seen in Figure 4.3 and Figure 4.4 below with a radius of 3.25 cm (the detector edge is at a 4.5 cm radius mentioned in Chapter 2).

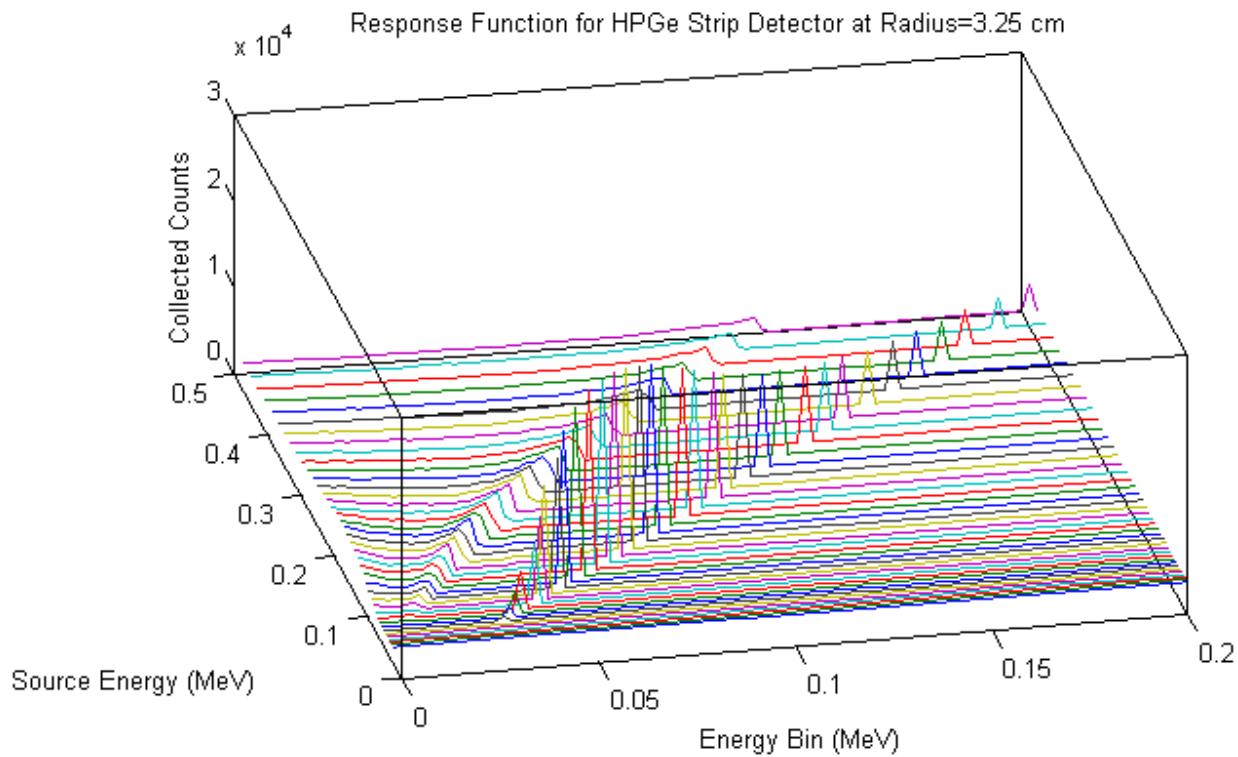


Figure 4.3: Response Function for the HPGe Strip detector at 3.25 cm Radius

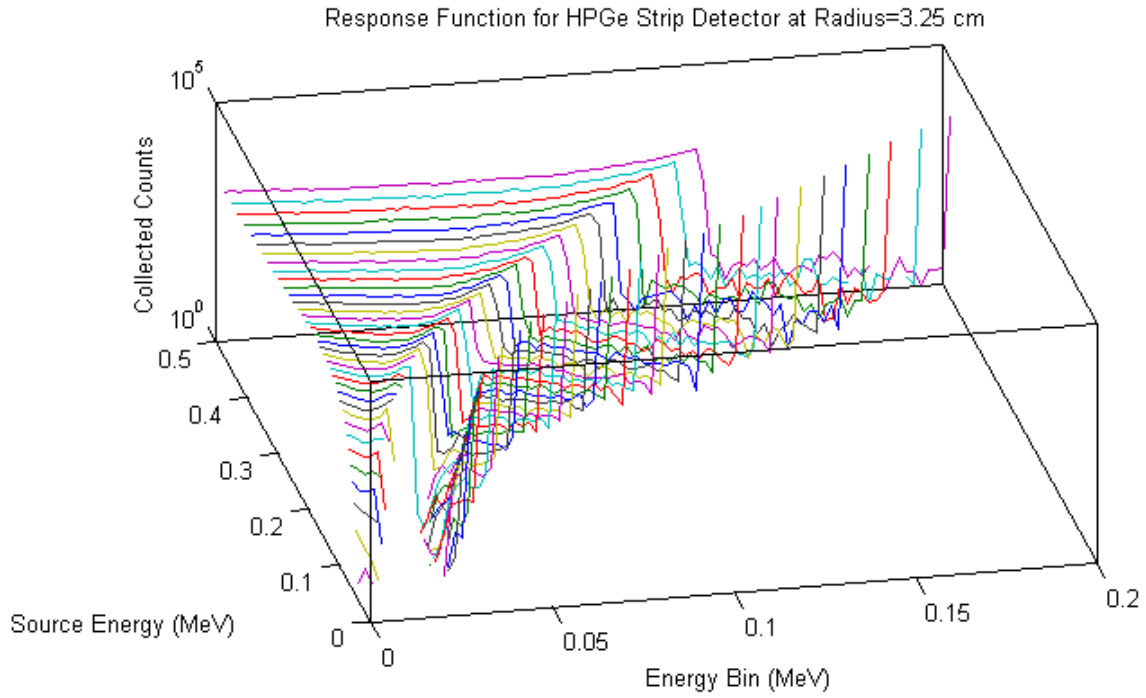


Figure 4.4: Response Function for the HPGe Strip detector at 3.25 cm Radius (Log Scale)

The full energy peak from the photoelectric effect is the dominant feature in these spectra. Since the Z value for Germanium is 32 and the energy range is from 0.05 to 0.5 MeV, the graph below substantiates that the full energy peak from the photoelectric effect is indeed the dominate feature in this regime.

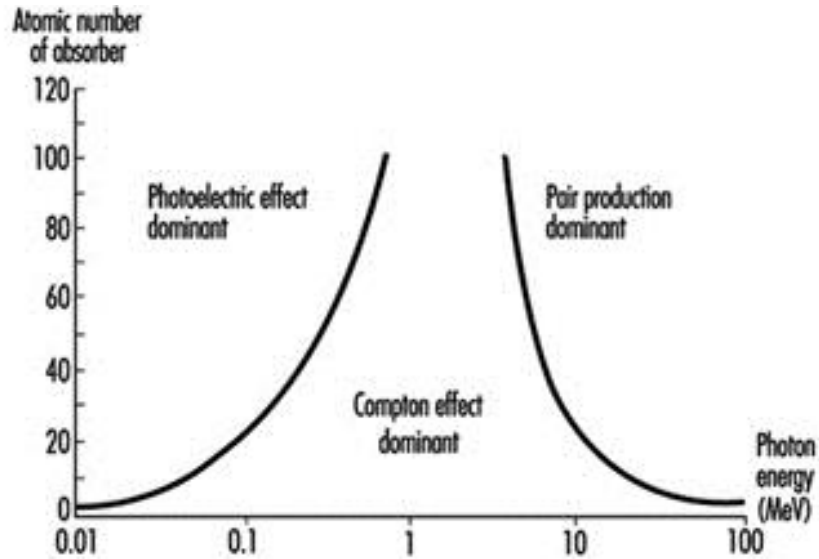


Figure 4.5: Dominating Photon Effects at Different Energy and in Different Material [28]

4.2 Single Energy and Radial Position Interpolated Spectra

A single source energy and radius not in the generated response function library was interpolated and re-binned to prove this interpolation method is accurate. An energy of 0.1635 MeV and a radius of 2.00 cm was interpolated and then compared with the MCNPX-PoliMi generated spectrum. The Compton edge and continuum begin at approximately 0.06 MeV. The results are shown below.

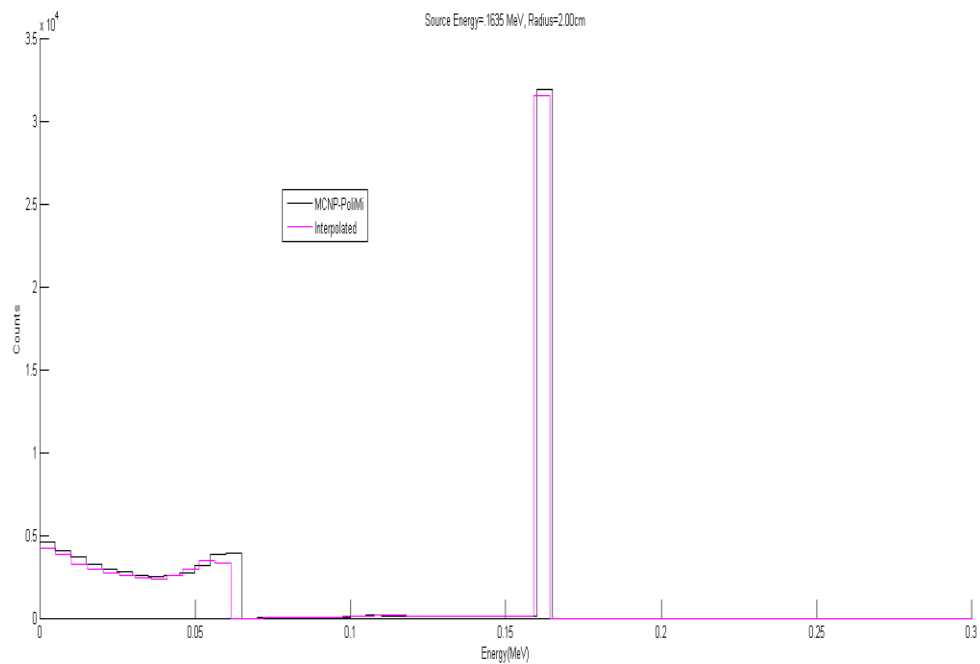


Figure 4.6: MCNPX-PoliMi Generated Spectrum vs Interpolated Spectrum Without Re-binning, Linear Scale

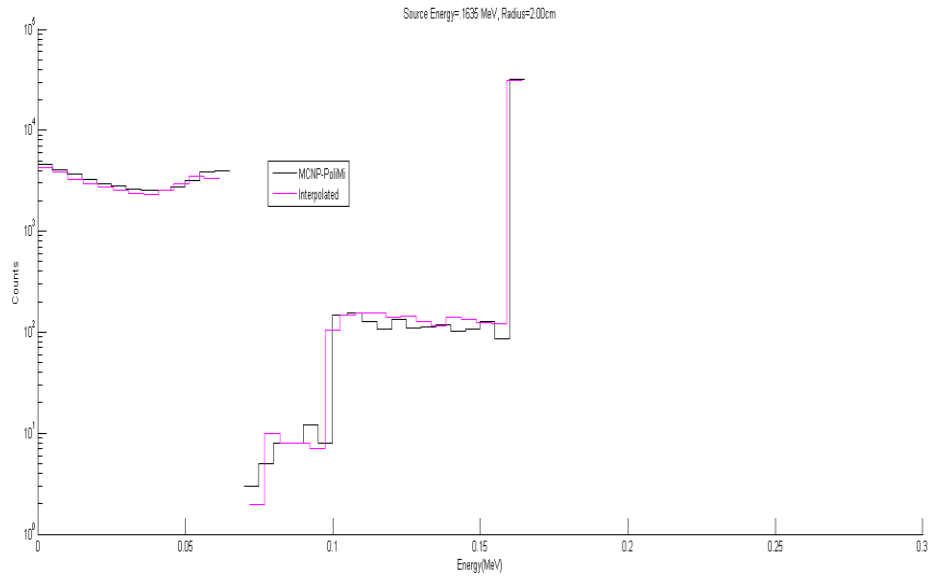


Figure 4.7: MCNPX-PoliMi Generated Spectrum vs Interpolated Spectrum Without Re-binning, Log Scale

Notice in Figure 4.7 that the discontinuity at the Compton edge derives from the lack of counts collected at this energy. Comparing the interpolated spectrum and the direct calculation reveals that the spectra are very similar. After the interpolated spectrum was re-binned, the final spectrum comparison is shown below for a single interpolated energy and radius.

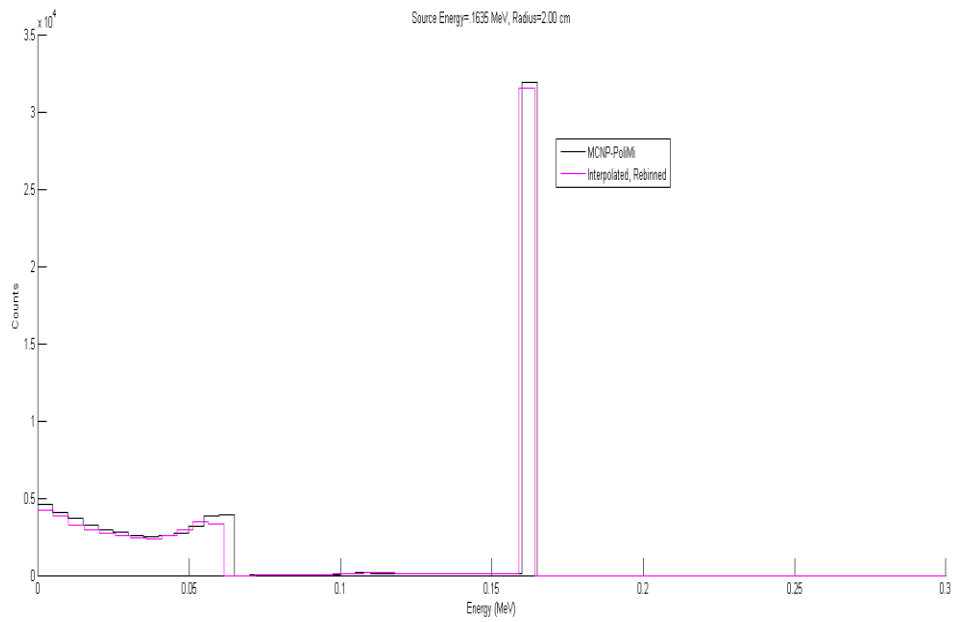


Figure 4.8: MCNPX-PoliMi Generated Spectrum vs Interpolated Spectrum with Re-binning,
Linear Scale

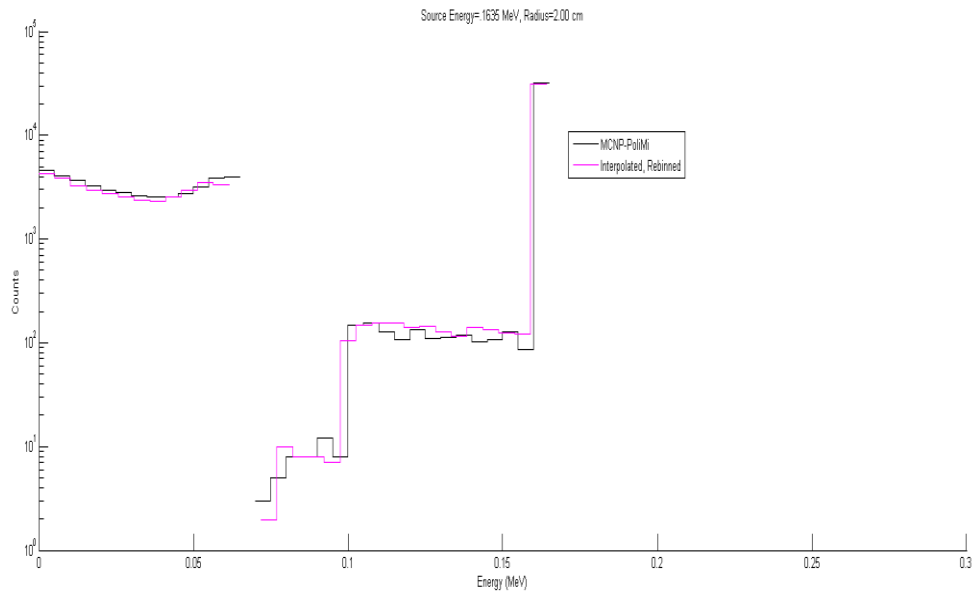


Figure 4.9: MCNPX-PoliMi Generated Spectrum vs. Interpolated Spectrum with Re-binning,
Log Scale

The difference between re-binning is small but necessary to compare the MCNPX-PoliMi calculation to the interpolated and re-binned spectrum. As expected, re-binning the data resulted in the data being spread across more energy bins.

4.3 Ba-133 Decay Spectrum Using Interpolation Method

To verify that this is the correct response function for the HPGe strip detector and that this interpolated and re-binning method is correct for generating a spectrum, a real source spectrum from a radionuclide was compared to the MCNPX-PoliMi direct calculation of the spectrum. The radionuclide chosen was ^{133}Ba since it has several gamma rays that fall in the

detector's energy range (50-500 keV). The decay scheme and gamma ray energy and intensities are given in Table 4.1 and Figure 4.10.

Table 4.1: Gamma Ray Energies and Intensities for ^{133}Ba [26].

<u>Gamma Ray Energy (keV)</u>	<u>Gamma Ray Intensity (%)</u>
53.1625	2.2
79.6139	2.6
80.9971	34
160.6109	0.64
223.2373	0.45
276.3997	7.16
302.851	18.3
356.0134	62
383.848	8.9

133BA EC DECAY (10.52 Y)

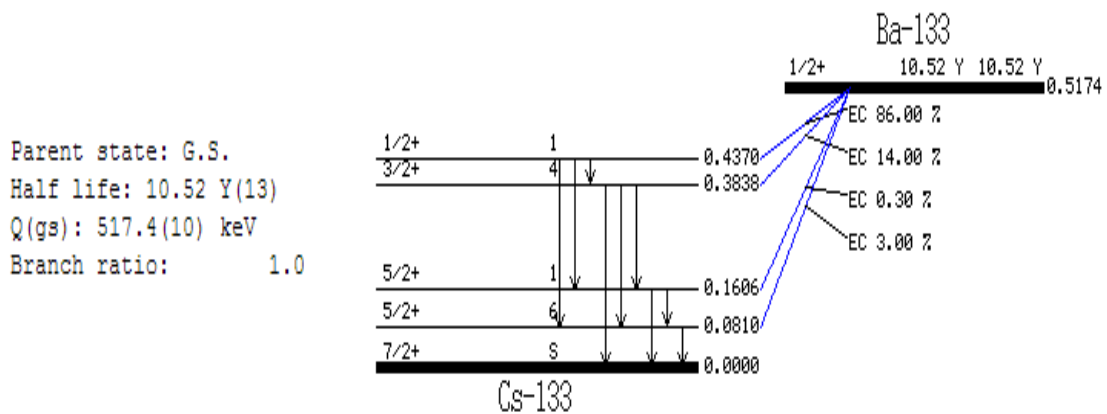


Figure 4.10: Decay Scheme for ^{133}Ba to ^{133}Cs [26].

These nine energies were run separately in MCNPX-Polimi, multiplied by their intensity, and then added together to get the full ^{133}Ba decay spectrum (Figure 4.11 and Figure 4.12).

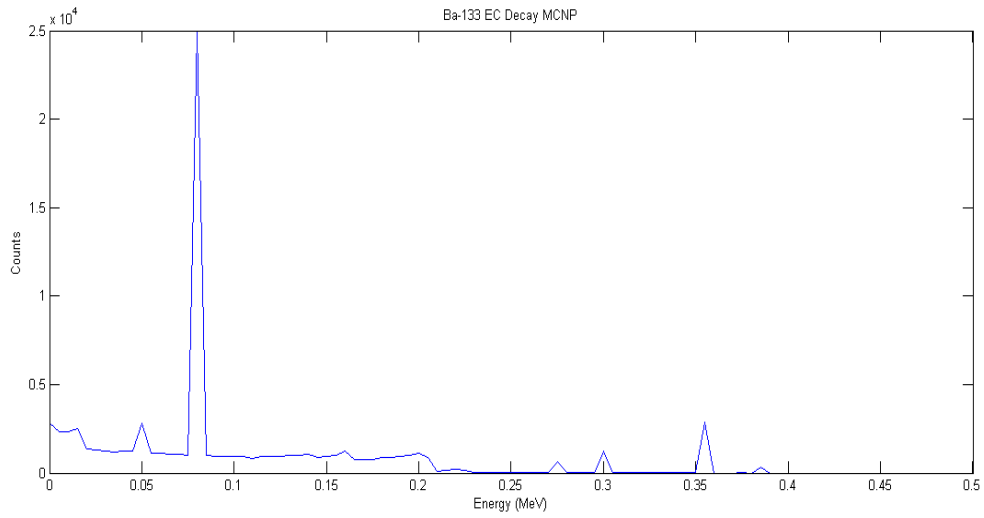


Figure 4.11: ^{133}Ba Decay Spectrum Calculated Using MCNPX-PoliMi

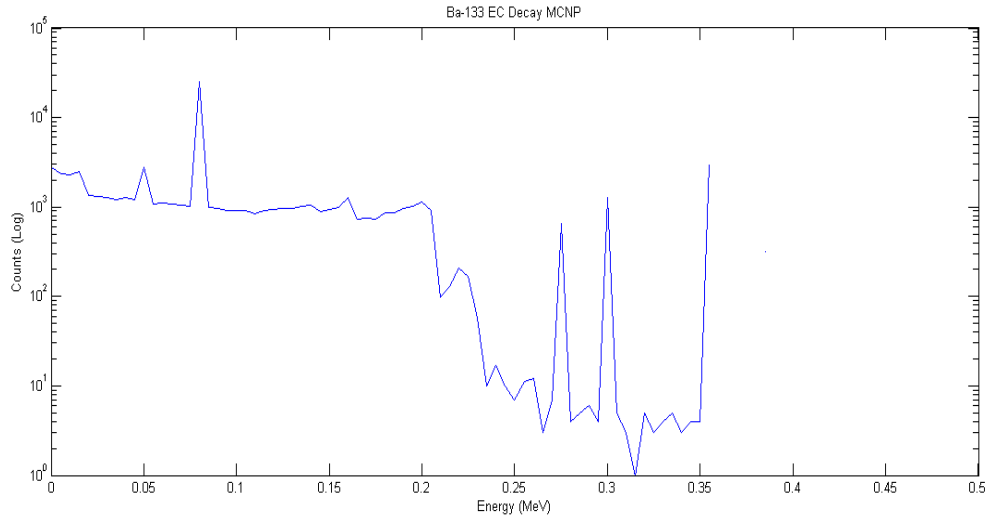


Figure 4.12: ^{133}Ba Decay Spectrum Calculated Using MCNPX-PoliMi (Log Scale)

Figure 4.13 demonstrates the typical Ba-133 spectrum found in practice and these peaks align correctly to the spectrum found in literature. The lowest energy peak, 0.053 MeV, does not show up in MCNPX-PoliMi generated spectrum as much because the lower energy photon does not have enough energy to strike both the front and back detector. If the photon is only stopped by the front detector, this will not register a count as mentioned previously.

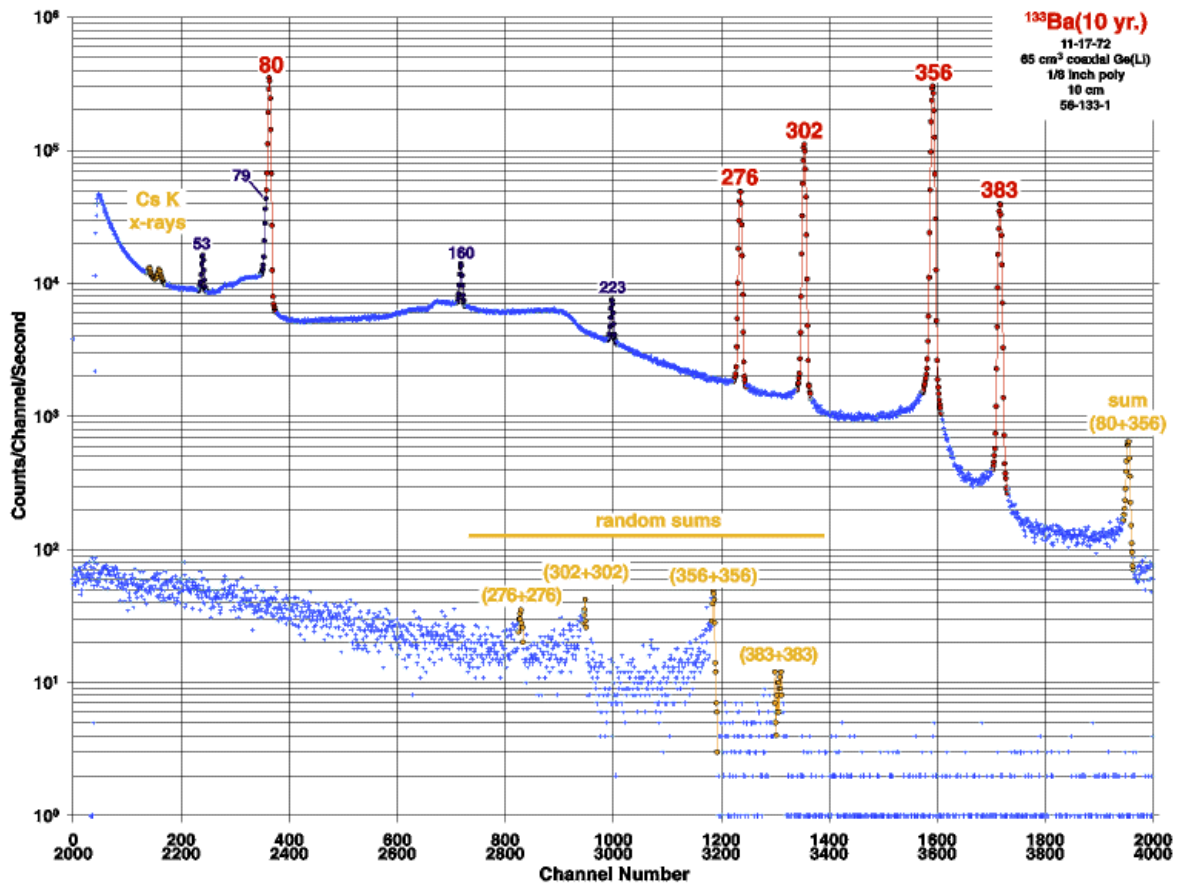


Figure 4.13: Germanium Spectrum of ^{133}Ba [27]

The result of these interpolations, with only energy being interpolated and the radius being a directly accessible in the library of interpolation data, is displayed in Figure 4.14 and Figure 4.15.

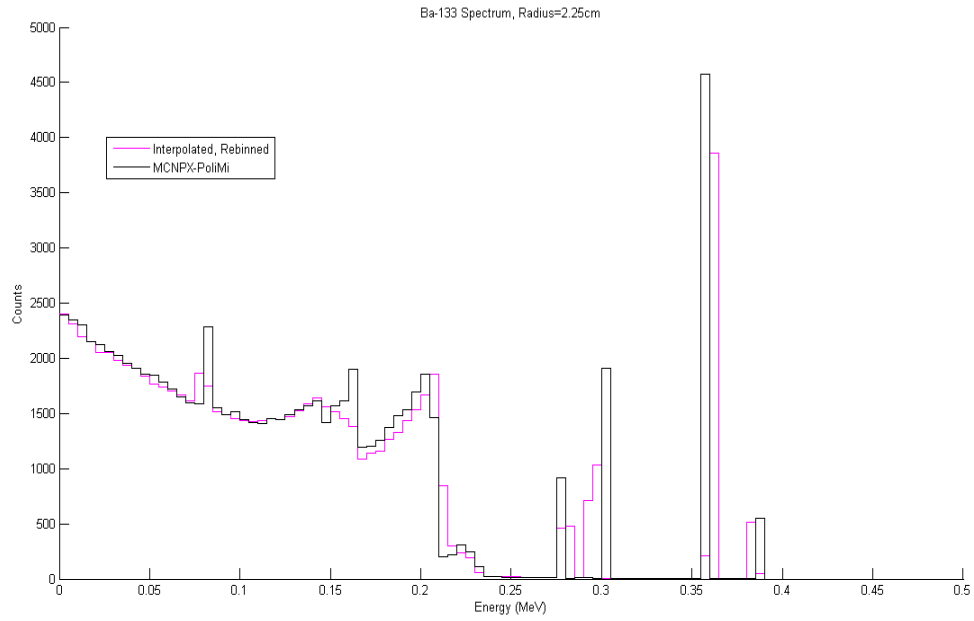


Figure 4.14: ^{133}Ba Spectrum Comparison with Interpolated and Re-binned Spectrum at a Radius of 2.25cm on a Linear Scale

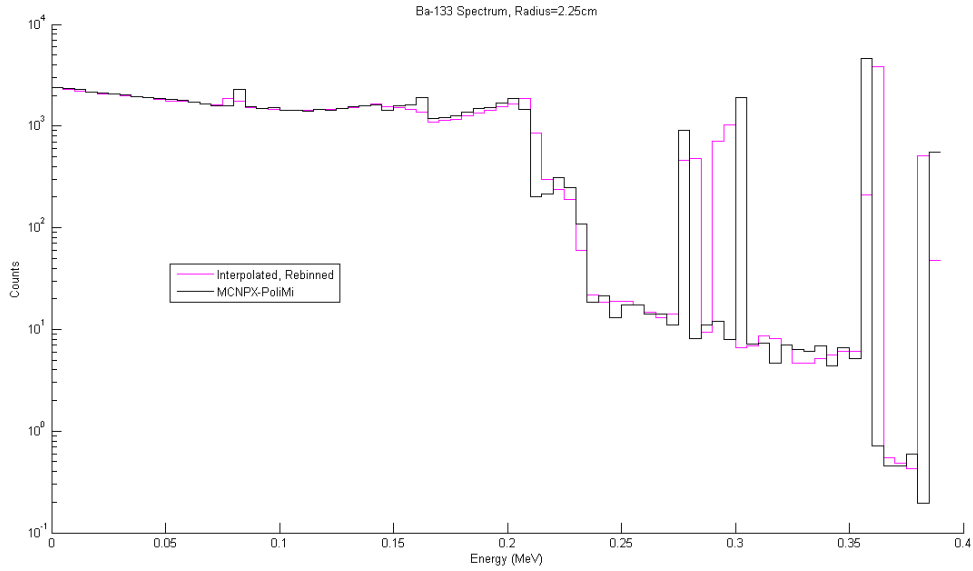


Figure 4.15: ^{133}Ba Spectrum Comparison with Interpolated and Re-binned Spectrum at a Radius of 2.25cm on a Log Scale

The interpolated and re-binned spectrum closely follows the direct calculation. The spread of the interpolated spectrum to the left of the 0.302 MeV energy was the result of the re-binning algorithm where the binning boundary fell such that only a few counts fell into the 0.302 MeV peak. These plots with error bars, using a Poisson distribution (square root of the counts), are shown below in Figures 4.16 and 4.17.

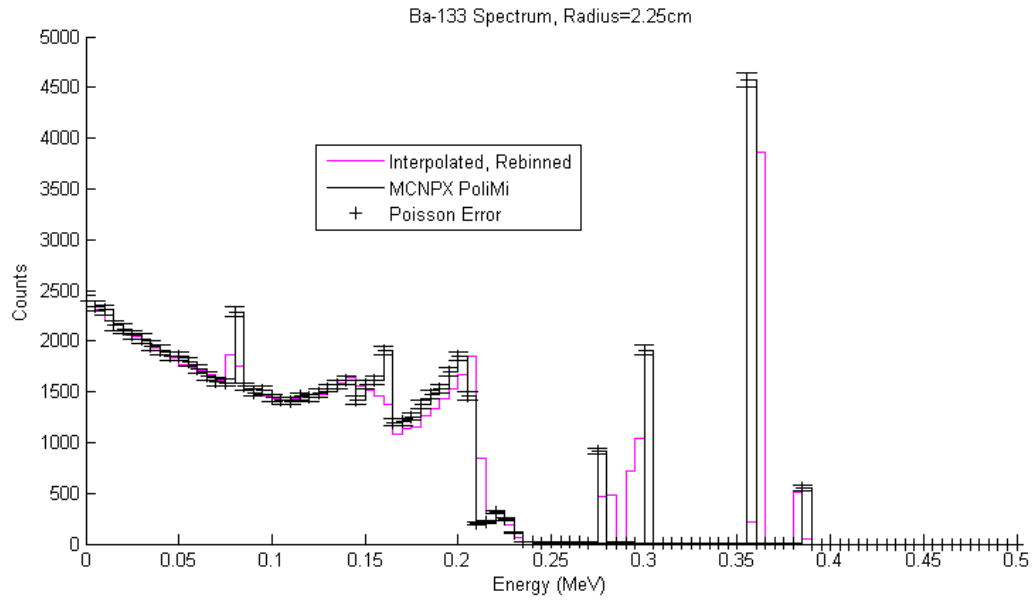


Figure 4.16: ^{133}Ba Spectrum Comparison with Interpolated and Rebinned Spectrum at a Radius of 2.25 cm on a Linear Scale, with Error Bars (Poisson)

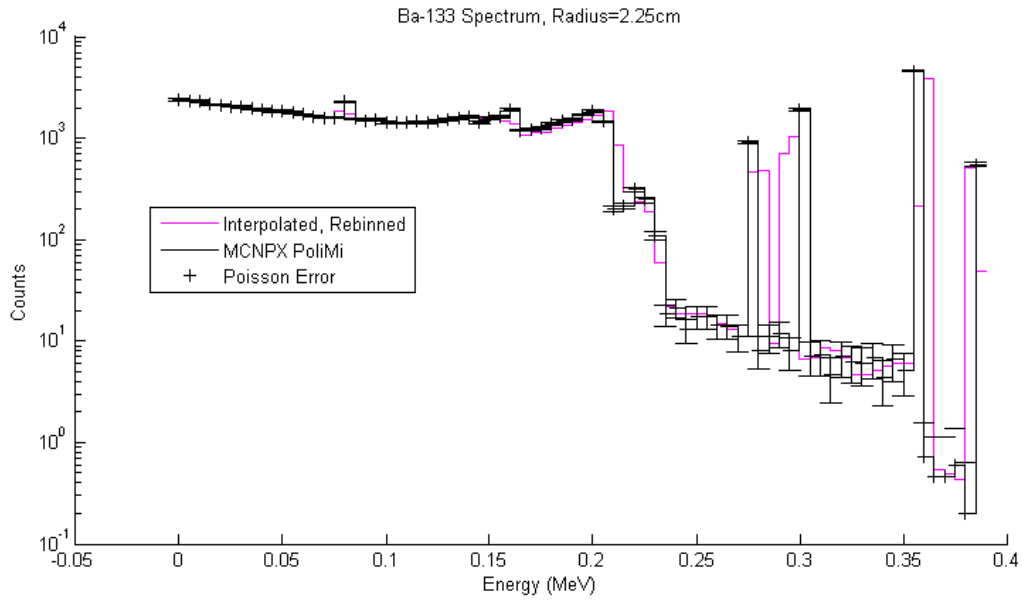


Figure 4.17: ^{133}Ba Spectrum Comparison with Interpolated and Rebinned Spectrum at a Radius of 2.35 cm on a Log Scale, with Error Bars (Poisson)

The ^{133}Ba spectrum was also compared with a radius that had to be interpolated (2.00cm). This radial distance was not already one of the radii already calculated in the interpolation library spectra. The result is shown below in Figures 4.18 and 4.19.

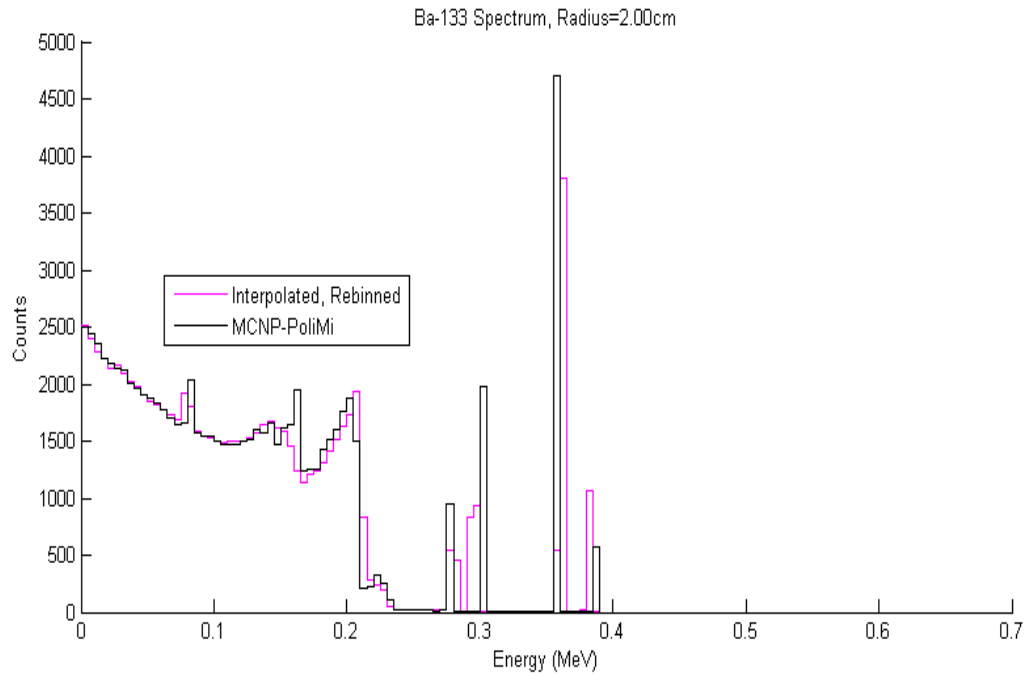


Figure 4.18: ^{133}Ba Spectrum Comparison with Interpolated and Rebinned Spectrum at a Radius of 2.00 cm on a Linear Scale

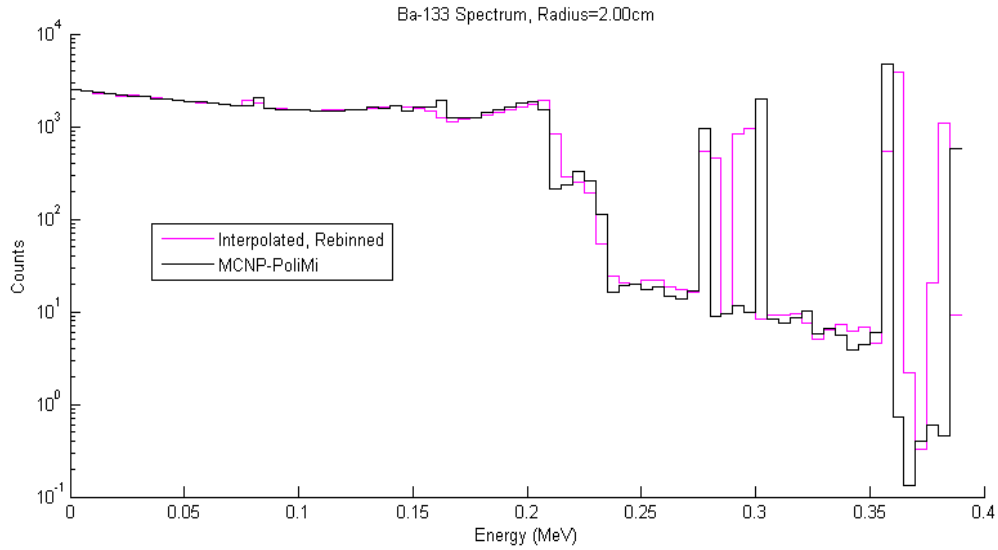


Figure 4.19: ^{133}Ba Spectrum Comparison with Interpolated and Re-binned Spectrum at a Radius of 2.00 cm on a Log Scale

These spectra are very similar but follow the direct calculation less closely than the spectrum where only energy was being interpolated. Since this interpolates both radius and energy, the results are not as accurate since there are now two dimensions interpolated. Again, the spreading issue at the 0.302 MeV peak is a result of the rebinning algorithm where the interpolated and MCNPX-PoliMi bin values greatly overlapped resulting in only a few counts making it to the bin that contains the 0.302 MeV peak. These results with error bars, using a Poisson distribution again, are shown below in Figures 4.20 and 4.21.

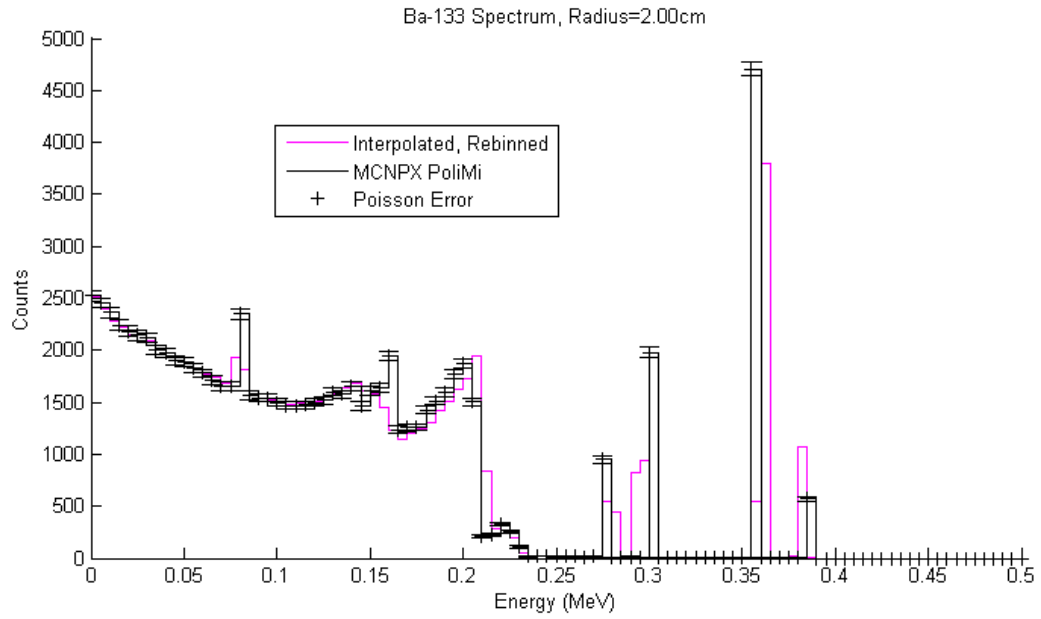


Figure 4.20: ^{133}Ba Spectrum Comparison with Interpolated and Re-binned Spectrum at a Radius of 2.00 cm on a Linear Scale, with Error Bars (Poisson)

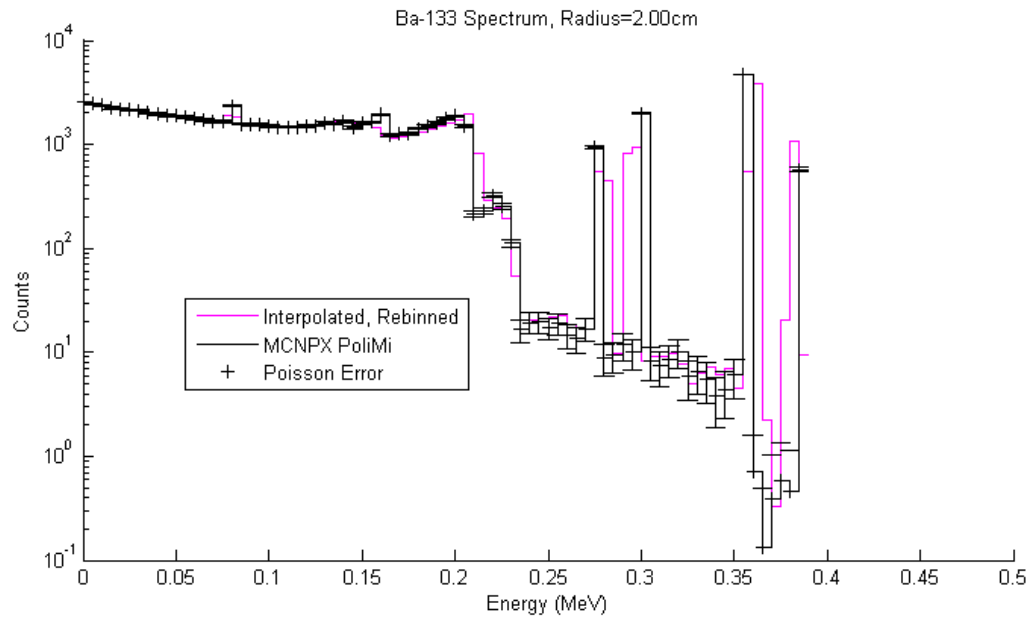


Figure 4.21: ^{133}Ba Spectrum Comparison with Interpolated and Re-binned Spectrum at a Radius of 2.00 cm on a Log Scale, with Error Bars (Poisson)

Chapter 5: Conclusions

This work on HPGe strip-type detector/imager has far reaching effects in many fields, especially in applications for homeland security and medical imaging. Position sensitive HPGe imagers like this give not only superior energy resolution with the gamma ray spectrum, but also information pertaining to the coordinates of the measured source. This project characterizes this type of detector using a model built in MCNPX PoliMi. The detector was determined to be radially symmetric in gamma ray counts. The generated photon interaction log was analyzed by photon features to create a detector response function versus radial position using 40 mono-energetic sources. These gamma ray spectra were then interpolated to create a detector response function that could be used to interpolate the response to an arbitrary source spectrum.

The main findings suggest that the single source energy interpolated spectrum in both the energy and radial position dimensions closely match the spectra directly calculated using MCNPX-PoliMi (Figures 4.8 and 4.9), showing this interpolation method is valid in this case. When comparing the Ba-133 decay spectrum in literature to that in the MCNPX PoliMi direct calculation for this detector setup (Figures 4.12 and 4.13), there were some notable differences. Namely, the lower gamma-ray energy at 0.053 MeV does not have enough energy to strike the front and back electrodes of the detector, therefore not registering a count as seen in these Ba-133 decay spectra that are being compared.

Comparing the interpolated method to the MCNPX PoliMi generated spectrum for Ba-133 decay with only the energy dimension being interpolated, the interpolated method

follows the general shape of the direct calculation (Figures 4.16 and 4.17). Similarly, adding the radial distance as an interpolation dimension yields a similar result with the interpolation method following the general shape of the direct calculation, albeit with more error due to the extra dimension being interpolated (Figures 4.20 and 4.21). Note that at the 0.302 MeV gamma ray energy, the re-binning algorithm has spread the counts in bins to the left of the actual direct calculation bin. Although this is rare, it can happen as a result of the sweep-style binning algorithm (Figure 3.22) where it is possible to have minimal overlap in the correct bin if the original bin structure falls in the new re-binning structure with only a few counts.

In order to expand on this research, a finer mesh of energy and pixels should be used. This project was limited by computational time due to access of only 32 cpus. The time for one MCNPX PoliMi run with one million particles took 5.61 minutes and with 40 energy points and 18 radius distances, this would take over 2 hours on 32 cpus. This was a reasonable amount of computational time on this project. However, since these counts are Poisson distributed and calculated with Monte Carlo methods where confidence is increased with more histories, decreasing the error by a factor of N requires the number of histories to be increased by N^2 which greatly increases computational time for small decreases in error. A smaller error would increase the validity of these calculations since the interpolation distances between energies and radii would be less coarse. In addition, experimental data should be compared to the computational data generated in this project. During the course of this research, the detector being studied was not available.

Overall, this research shows that by combining the detector symmetry in the radial direction and using an interpolation method for determining gamma ray spectra,

computational time can be hugely decreased compared to that of direct Monte Carlo methods.

REFERENCES

1. Doyle, James E. *Nuclear Safeguards, Security and Nonproliferation: Achieving Security with Technology and Policy*. Amsterdam: Butterworth-Heinemann, 2008. Print.
2. Burr, T., J. Gattiker, K. Myers, and G. Tompkins. "Alarm Criteria in Radiation Portal Monitoring." *Applied Radiation and Isotopes* 65.5 (2007): 569-80. Print.
3. Ziock, Klaus-Peter; Boehnen, Chris; Hayward, Jason; Raffo-Caiado, Ana C. "A Mechanically Cooled, Highly Portable, HPGe-based, Coded-Aperture Gamma-Ray Imager". Oak Ridge National Laboratory, Oak Ridge, TN. Proc. of 51st INMM Annual Meeting, Baltimore, MD, July 2010.
4. Fenimore, E.E.; Cannon, T. M., "Coded Aperture Imaging With Uniformly Redundant Arrays," *Applied Optics* Vol.17, No. 3 p337-347. 1 February 1978.
5. Lindsay C Johnson et al. "Characterization of a high-purity germanium detector for small-animal SPECT". *Physics in Medicine and Biology* Volume 56 Number 18 2011 *Phys. Med. Biol.* 56 5877 doi:10.1088/0031-9155/56/18/007
6. Tom Burr & Michael S. Hamada (2013) Moving Neutron Source Detection in Radiation Portal Monitoring, *Technometrics*, 55:3, 296-308, DOI: 10.1080/00401706.2013.775909

7. Kramer D. New radiation detectors for US ports leave lawmakers skeptical. *Physics Today* [serial online]. April 2008;61(4):32-35. Available from: Computers & Applied Sciences Complete, Ipswich, MA. Accessed January 7, 2014
9. Keyser, R. M., Hensley, W. W., Twomey, T. R., & Upp, D. L. (2008). Comparison of MCNP and experimental measurements for an HPGe-based spectroscopy portal monitor. *Journal Of Radioanalytical & Nuclear Chemistry*, 276(2), 399-405. doi:10.1007/s10967-008-0518-9
10. Kutz, G. (2006). Border Security: Investigators Successfully Transported Radioactive Sources Across Our Nation's Borders at Selected Locations: GAO-06-545R. *GAO Reports*, 1.
11. Leeney, M. (2009). Fast quaternion slerp. *International Journal Of Computer Mathematics*, 86(1), 79-84. doi:10.1080/00207160801923064
12. "Alec's Web Log." *Alecs Web Log*. WordPress, 12 Apr. 2010. Web. <http://www.alecjacobson.com/weblog/?p=981>.
13. Faw, Richard E., and J. Kenneth Shultis. *An MCNP Primer*. Manhattan, KS: Dept. of Mechanical and Nuclear Engineering Kansas State University, 2004-2011. Print.

14. Jhykes. "Rebin.py." *GitHub*. GitHub, n.d. Web. 23 Mar. 2014.
15. Knoll, Glenn F. *Radiation Detection and Measurement*. 4th ed. Hoboken, NJ: John Wiley, 2010. 365, 416-17. Print.
16. Shultis, J. Kenneth., and Richard E. Faw. *Fundamentals of Nuclear Science and Engineering*. 2nd ed. Boca Raton: CRC, 2008. 232-36. Print.
17. Vetter, K., L. Mihailescu, K. Ziok, M. Burks, C. Cork, L. Fabris, E. Hull, N. Madden, and R. Pehl. "Employing Thin HPGe Detectors for Gamma-ray Imaging." *Lawrence Livermore National Laboratory* (2002): 129-34. *EBSCO*. Web.
18. Ziock, Klaus P., M. T. Burks, W. Craig, L. Fabris, E. L. Hull, and N. W. Madden. "Real-time Generation of Images with Pixel-by-pixel Spectra for a Coded Aperture Imager with High Spectral Resolution." *Nuclear Instruments and Methods in Physics Research A.505* (2003): 420-24. *Science Direct*. Web.
19. Peköz, Rengin, and Cüneyt Can. "Components of Detector Response Function: Monte Carlo Simulations and Experiment." *X-Ray Spectrometry* 35.6 (2006): 347-51. Print.
20. Jiaxin Wang, Zhijian Wang, Johanna Peebles, Huawei Yu, Robin P. Gardner, Development of a simple detector response function generation program: The CEARDRFs

code, *Applied Radiation and Isotopes*, Volume 70, Issue 7, July 2012, Pages 1166-1174, ISSN 0969-8043, <http://dx.doi.org/10.1016/j.apradiso.2011.11.003>.
(<http://www.sciencedirect.com/science/article/pii/S0969804311005380>)

21. Tsoufanidis, Nicholas. *Measurement and Detection of Radiation*. Washington, DC: Taylor & Francis, 1995. 304-05. Print.

22. Metwally, W. A., R. P. Gardner, and Avneet Sood. "Gaussian Broadening of MCNP Pulse Height Spectra." *Transactions of the American Nuclear Society* 91 (2004): 789-90. Web.

23. Blackston, Matthew. (2012). Personal communication, Oak Ridge National Laboratory, TN.

24. Holmgren, Casper. Hs-rebin. GitHub repository. <https://github.com/icasperzen/hs-rebin>.

25. Souvaine, Diane. "Line Segment Intersection Using a Sweep Line Algorithm". 2008. http://www.cs.tufts.edu/comp/163/notes05/seg_intersection_handout.pdf.

26. Shaheen Rab, *Nuclear Data Sheet* 75,491 (1995). atom.kaeri.re.kr/ton/.

27. "Germanium Spectrum of Barium-133, New Plot of Original Data Incorporating ENSDF Data." *Spectrum Catalog Samples* (2005): n. pag. *Idaho National Laboratory*. Web. 2 June 2014. <<http://www.inl.gov/gammaray/catalogs/ba133.shtml>>.
28. Cherry Jr., Robert N., 48. *Radiation: Ionizing*, Cherry Jr., Robert N., Editor, *Encyclopedia of Occupational Health and Safety*, Jeanne Mager Stellman, Editor-in-Chief. International Labor Organization, Geneva. © 2011.
http://www.ilo.org/oshenc/images/stories/Part06/ION_imgs/ION010F1.jpg.
29. Elleman TS, Mayo RM, Peplow DE, Stam E. 2009. Gamma-Ray Spectroscopy. In: Hawari AI, Harp JM, editors. *Gamma-Ray Spectroscopy*, Raleigh (NC): NCSU. p 1-9.
30. Mayo RM, Peplow DE. 2009. Statistical Models and Uncertainty Analysis. In: Hawari AI, Harp JM, editors. *The Gieger-Muller Detector, Statistical Models and Uncertainty Analysis*. Raleigh (NC): NCSU. p 1-8.
31. "Main Page/PHYS 4210/Gamma Ray Spectroscopy." *Physics Wiki*. MediaWiki, 11 Mar. 2014. Web. 03 June 2014.
<http://physwiki.apps01.yorku.ca/index.php?title=Main_Page/PHYS_4210/Gamma_Ray_Spectroscopy>.

32. "Semiconductor Detectors." *Nuclear Safeguards Education Portal*. Texas A&M University Department of Nuclear Engineering, 2014. Web. 3 June 2014. <<http://nsspi.tamu.edu/nsep/courses/basic-radiation-detection/semiconductor-detectors/introduction/introduction>>.
33. Guttormsen, M., T. S. Tveter, L. Bergholt, F. Ingebretsen, and J. Rekstad. "The Unfolding of Continuum Gamma-ray Spectra." *Nuclear Instruments and Methods in Physics Research A*.374 (1996): 371-76. Web.
34. Ziock, Klaus P., Norm Madden, Ethan Hull, William Craig, Tony Laviertes, and Chris Cork. "A Germanium-Based, Coded Aperture Imager." *Institute of Electrical and Electronics Engineers* (2002): 864-68. Web
35. Minoru, Oda. "High-Resolution X-Ray Collimator with Broad Field of View for Astronomical Use." *Applied Optics* 4.1 (1965): 143. *Optics InfoBase: Applied Optics*. Web. 04 June 2014. <<http://www.opticsinfobase.org/ao/abstract.cfm?URI=ao-4-1-143>>.
36. Padovani, Enrico. Pozzi, Sarah A. Clarke, Shaun D. Miller, Eric C. Introduction to MCNPX-PoliMi. Politecnico di Milano, Milan, Italy, University of Michigan, Ann Arbor, Mi, USA.

37. Ziock, K.P.; Blackston, M.A.; VanVuure, T., "3D Millimeter Event Localization in Bulk Scintillator Crystals," *Nuclear Science, IEEE Transactions on* , vol.60, no.2, pp.1390,1399, April 2013 doi: 10.1109/TNS.2013.2251353
38. "Sizes: Using a Pinhole Camera to Measure the Sun or Moon." Department of Physics - Educational Outreach. Department of Physics at University of Cambridge, 2008. Web. 04 June 2014. <<http://www-outreach.phy.cam.ac.uk/resources/astro/KS3/sizes/index.php>>.
39. Pozzi, Sara, Enrico Padovani, and Marzio Marseguerra. "MCNP-PoliMi: A Monte-Carlo Code for Correlation Measurements." *Nuclear Instruments and Methods in Physics Research A*.513 (2003): 550-58. Web
40. Farrell, Joyce. "Resolution and Light Sensitivity Tradeoff with Pixel Size." (n.d.): n. pag. Stanford University, Stanford, CA *Agilent Technologies, Santa Clara, CA. Web. 9 July 2014.<<http://www.invensense.com/cn/mems/gyro/documents/articles/ResolutionandLightSensitivityTradeoffWithPixelSize.pdf>>.
41. Jin, Y., R. P. Gardner, and K. Verghese. "A Semi-Empirical Model for the Gamma-Ray Response Function of Germanium Detectors Based on Fundamental Interaction Mechanisms." *Nuclear Instruments and Methods in Physics Research A*242 (1986): 416-26. Web.